Lab on a Chip

CRITICAL REVIEW

View Article Online
View Journal | View Issue

Cite this: *Lab Chip*, 2023, **23**, 1226

Label-free microfluidic cell sorting and detection for rapid blood analysis

Nan Lu, [ab] Hui Min Tay, [a] Chayakorn Petchakup, [a] Linwei He,[a] Lingyan Gong,[a] Kay Khine Maw, [a] Sheng Yuan Leong,[a] Wan Wei Lok,[a] Hong Boon Ong,[a] Ruya Guo,[c] King Ho Holden Li [ab] and Han Wei Hou *[abd]

Blood tests are considered as standard clinical procedures to screen for markers of diseases and health conditions. However, the complex cellular background (>99.9% RBCs) and biomolecular composition often pose significant technical challenges for accurate blood analysis. An emerging approach for point-of-care blood diagnostics is utilizing "label-free" microfluidic technologies that rely on intrinsic cell properties for blood fractionation and disease detection without any antibody binding. A growing body of clinical evidence has also reported that cellular dysfunction and their biophysical phenotypes are complementary to standard hematoanalyzer analysis (complete blood count) and can provide a more comprehensive health profiling. In this review, we will summarize recent advances in microfluidic label-free separation of different blood cell components including circulating tumor cells, leukocytes, platelets and nanoscale extracellular vesicles. Label-free single cell analysis of intrinsic cell morphology, spectrochemical properties, dielectric parameters and biophysical characteristics as novel blood-based biomarkers will also be presented. Next, we will highlight research efforts that combine label-free microfluidics with machine learning approaches to enhance detection sensitivity and specificity in clinical studies, as well as innovative microfluidic solutions which are capable of fully integrated and label-free blood cell sorting and analysis. Lastly, we will envisage the current challenges and future outlook of label-free microfluidics platforms for high throughput multi-dimensional blood cell analysis to identify non-traditional circulating biomarkers for clinical diagnostics.

Received 27th September 2022,
Accepted 10th January 2023

DOI: 10.1039/d2lc00904h

rsc.li/loc

Introduction

Blood is the most complex biofluid in our body and consists of a diverse range of circulating cell types (red blood cells (RBCs), white blood cells (WBCs), platelets, *etc.*) and biomolecules (lipids, proteins and nuclei acids) that reflect our health and disease status.[1] Routine blood testing is considered a standard clinical procedure in the diagnosis of many diseases. A typical clinical blood test measures your complete blood count (CBC), metabolic and lipid profiles, and hormone levels to detect pathological conditions including diabetes, cancer and anemia.[2,3] While CBC using hematoanalyzers can detect the presence of infections based on cell enumeration or the neutrophil–lymphocyte ratio,[4] increasing clinical evidence has shown that probing of cellular functions,[5,6] biophysical phenotypes,[7,8] and non-traditional cellular markers (*e.g.* monocyte–platelet aggregates[9]) is more comprehensive and invaluable in disease detection (*e.g.* sepsis and COVID-19 (ref. 10–12)). Platelet activation is also observed in viral infections such as human immunodeficiency virus (HIV),[13,14] hepatitis C virus (HCV)[15] and dengue,[16,17] with thrombocytopenia as a clinical hallmark in dengue patients. Besides immune cells, diseased cells such as circulating tumor cells (CTCs) are present in blood during cancer metastasis which are crucial for cancer prognosis, diagnosis and treatment monitoring.[18,19]

Apart from cellular components, there is increasing interest in studying cell-derived extracellular vesicles (EVs) and their roles in cell–cell communication and disease pathophysiology.[20] Circulating EVs (exosomes and microvesicles) in blood often contain disease-specific information from their host cells, making them ideal biomarkers for non-invasive liquid biopsy[21] in inflammation and injury,[22–24] diabetes,[21] CVD,[25] cancer[26] and COVID-19.[27]

[a] *School of Mechanical and Aerospace Engineering, Nanyang Technological University, 50 Nanyang Avenue, Blk N3, Level 2, Room 86 (N3-02c-86), 639798, Singapore. E-mail: hwhou@ntu.edu.sg; Tel: +65 67904950*
[b] *HP-NTU Digital Manufacturing Corporate Lab, Nanyang Technological University, 65 Nanyang Drive, Block N3, 637460, Singapore*
[c] *Key Laboratory of Agricultural Information Acquisition Technology, Ministry of Agriculture and Rural Affairs, China Agricultural University, Beijing, 100083, China*
[d] *Lee Kong Chian School of Medicine, Nanyang Technological University, 11 Mandalay Road, Clinical Sciences Building, 308232, Singapore*

Recent technological advances have also demonstrated EV-based diagnosis for cancer,[28–30] Alzheimer's disease[31] and Parkinson's disease[32] with superior detection sensitivity to conventional testing methods. Due to their nanoscale sizes (~50 nm–1 μm),[33] EV isolation remains a major bottleneck and researchers are actively developing novel tools and assays to study EV biology and improve their clinical adoption.

While blood possesses numerous cell types and components which makes it a rich source of biomarkers, these cells and components can in turn increase the complexity of analysis as the high content of cellular components (~50% v/v) and RBC abundance (>99% of all cells) pose significant technical challenges for many blood tests and diagnostics. For example, the scarcity of circulating tumor cells (CTCs) in blood (1–100 CTCs among billions of RBCs)[34,35] is a major bottleneck for CTC isolation and detection. This is further aggravated by pre-treatment steps such as centrifugation and RBC lysis which could cause cell loss.[36] Conventional sample preparation steps (*e.g.* centrifugation, density gradient centrifugation) are time consuming, laborious and could also cause unnecessary activation of sensitive immune cells,[6] platelet activation[37] and shear-induced microparticle shedding.[38] Other approaches such as immunocapture using antibodies could alter cell function or phenotype which complicates downstream analysis.[34] Therefore, fast and efficient blood separation methods are highly sought after to gain deeper insights into their biophysiological functions and empower clinicians with more comprehensive blood analysis. Microfluidics has revolutionized biomedical research with unprecedented sensitivity and efficiency by enabling small blood volume handling and precise control of the cell microenvironment. In particular, label-free microfluidic approaches which utilize intrinsic cell properties for cell separation and detection (without using antibodies) are extremely attractive for low-cost and rapid diagnostics. Recently, a plethora of technologies have been reported for label-free blood cell sorting based on cell size, shape, density and deformability. As these cellular biophysical properties are commonly linked to cell biology and pathology,[39] they can be further exploited for label-free cell phenotyping to identify cell diseases and cellular states[40] including lymphocyte activation,[41] sepsis,[42] diabetes[43] and renal diseases.[44]

While several reviews have been published on microfluidic cell-sorting techniques,[45,46] and single cell analysis,[47–49] in this review, we aim to provide a comprehensive overview on recent microfluidics technologies (selecting publications after 2015) for label-free blood cell separation and detection. We will first focus on various blood fractionation techniques for microscale (WBCs, platelets) and nanoscale (EVs) blood components (Fig. 1). We will next summarize the applications of single cell analysis for label-free detection (optical, mechanical and electrical) of cellular properties as novel blood-based biomarkers in diseases (Fig. 8). Thirdly, we will discuss machine learning approaches used for multi-parametric cell profiling, and showcase integrated microfluidic platforms that achieve complete label-free blood cell sorting and analysis. Lastly, we will offer our perspectives on the challenges and future directions of microfluidic-based label-free blood diagnostics.

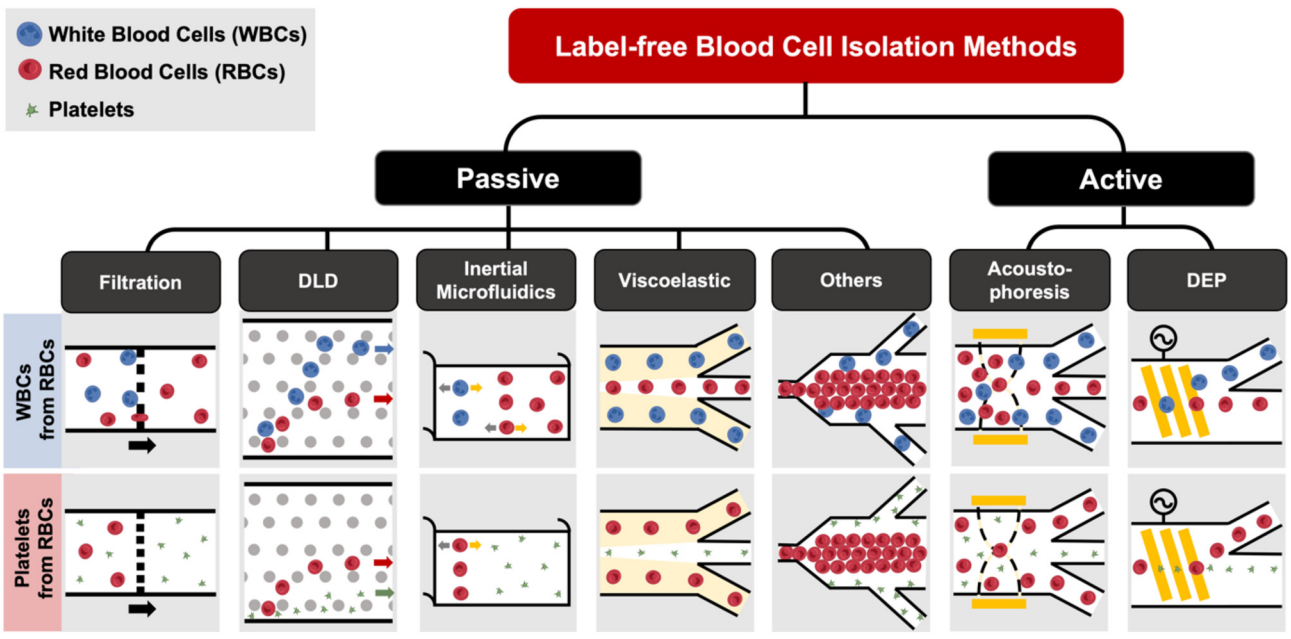

Fig. 1 Overview of label-free blood cell sorting categorized as passive (filtration, deterministic lateral displacement (DLD), inertial microfluidics, viscoelastic) and active (acoustophoresis and dielectrophoresis) methods.

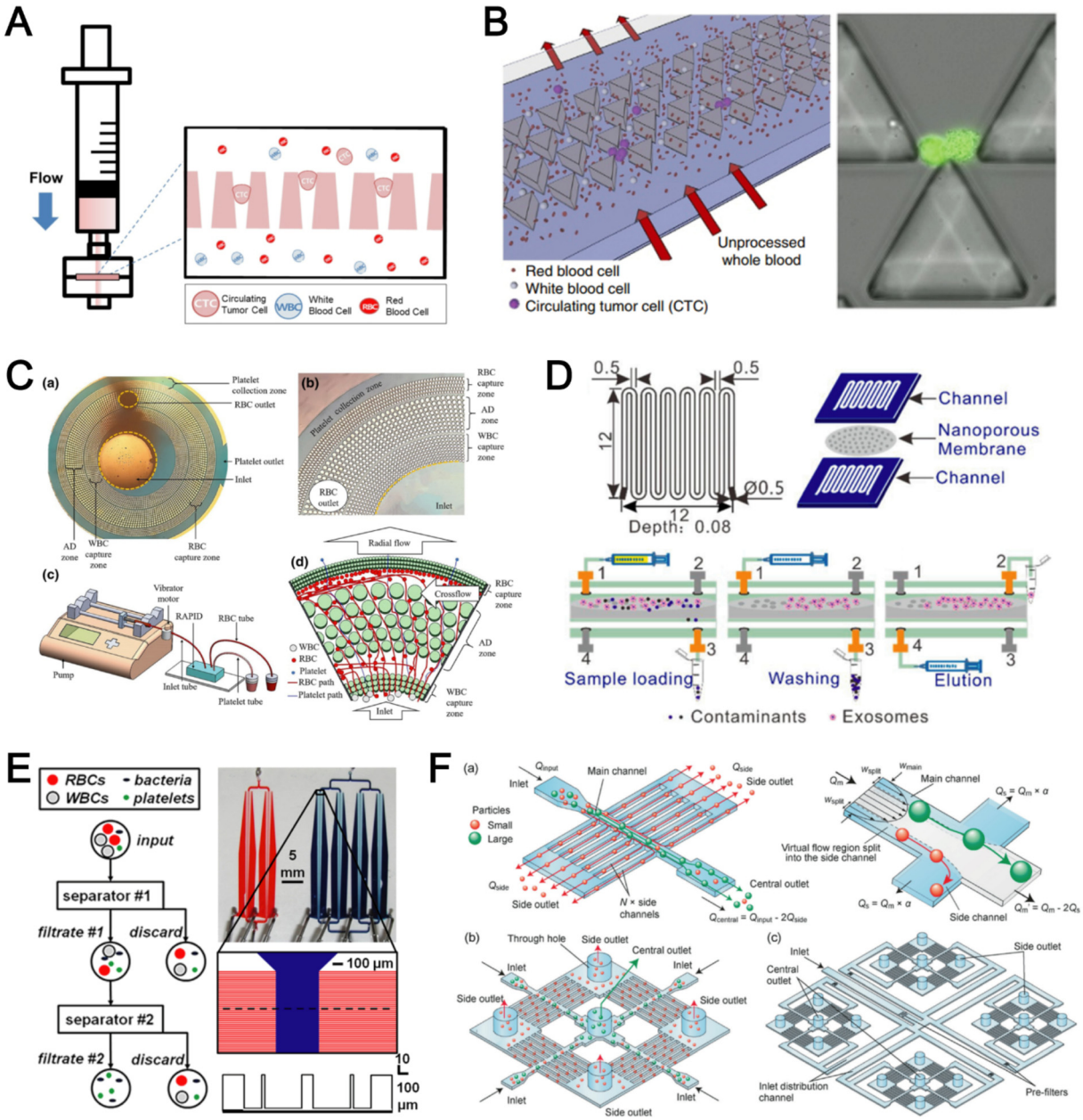

Fig. 2 Microfluidic filtration cell sorting. (A) CTC isolation using a tapered-slit filter fabricated with a photosensitive polymer device. Reproduced from ref. 64 with permission from Ivyspring International Publisher. (B) Schematic of the cluster-chip with triangular pillars for CTC cluster isolation. Reproduced from ref. 65 with permission from Springer Nature. (C) High throughput radial pillar device for platelet enrichment. (a) Microscope image of the device; (b) magnified image of a sector of the device shows the varying sizes of the pillars and the pillar gaps in each of the three zones; (c) schematic of the experimental set-up for platelet enrichment from whole blood; (d) schematic of the radial, and the cross flows. Reproduced from ref. 66 with permission from Springer Science + Business Media. (D) Microfluidic tangential flow filtration, or cross-flow filtration device for exosome isolation and purification. Reproduced from ref. 75 with permission from Elsevier. (E) Microfluidic cross-flow device for bacteria separation from diluted whole blood. Reproduced from ref. 72 with permission from Elsevier. (F) Schematic of the numbering-up chip for direct leukocyte and erythrocyte separation. (a) A separation unit for particle sorting and particle behaviors at a branch point; (b) a square, integrated structure composed of 4 separation units; (c) four arranged structures shown in image (b) connected to a symmetrically branched inlet distribution channel. Reproduced from ref. 70 with permission from the Royal Society of Chemistry.

Label-free blood fractionation

Conventional cell sorting methods include physical filtration,[50,51] density gradient centrifugation (*e.g.* Ficoll or Percoll),[52] and addition of labels to identify target cells prior to isolation.[53] The current gold standard is fluorescence activated cell sorting (FACS)[51,54] which uses flow cytometry to detect fluorescently-labelled cells and sort them into different populations based on surface marker expression. Another popular approach is magnetic activated cell sorting (MACS)[53–55] that uses antibodies conjugated with magnetic labels for positive or negative cell selection. Despite the high specificity and separation efficiency of these techniques, they are mostly limited for research use due to laborious

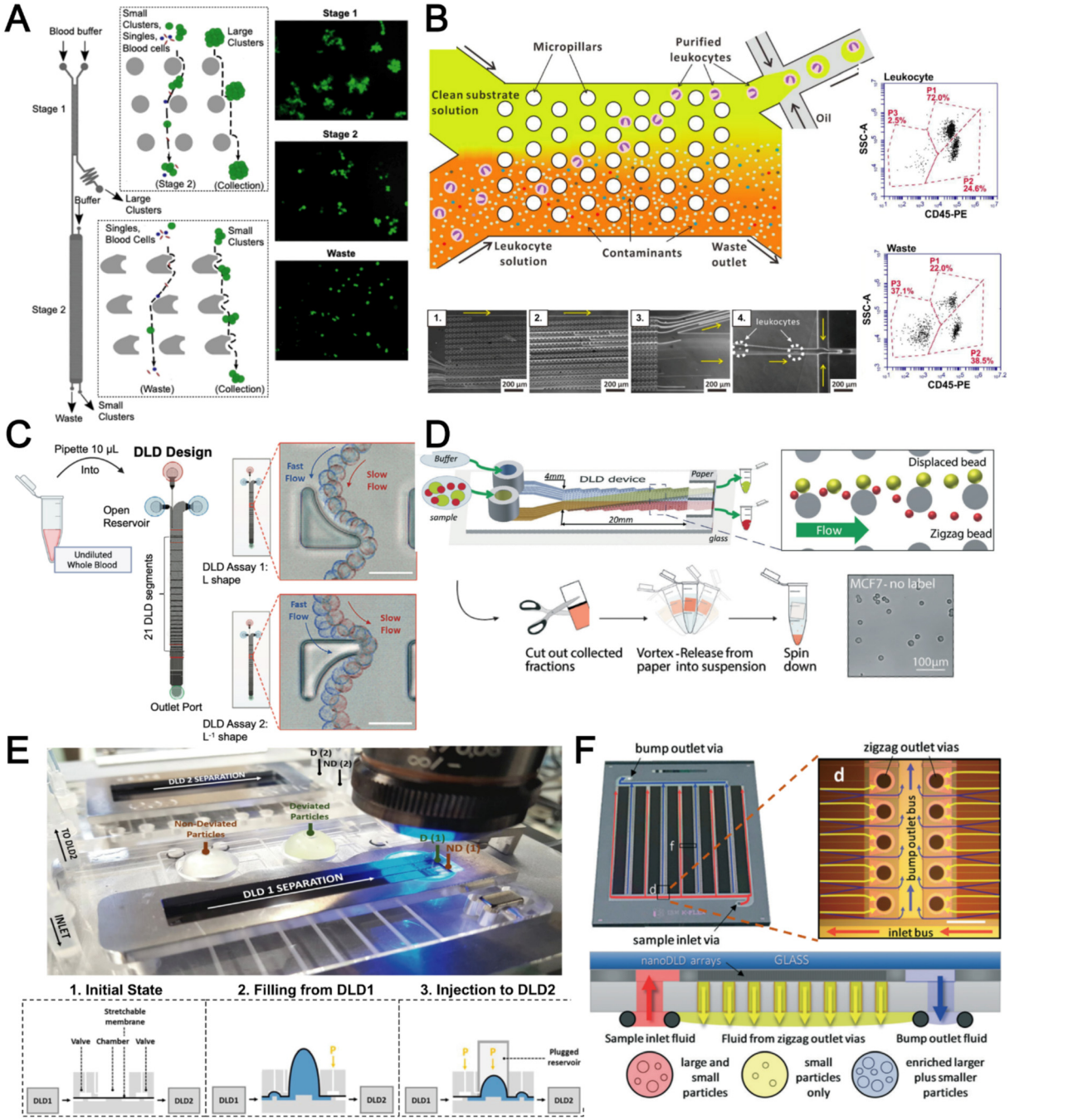

Fig. 3 Deterministic lateral displacement (DLD). (A) Schematic representation of a cascaded DLD array device for isolation of large and small CTCs clusters. Reproduced from ref. 79 with permission from Nature Research. (B) An integrated continuous-flow microfluidic assay to separate leukocytes from lysed blood solution and resuspension in clean substrate solution for subsequent droplet encapsulation. Reproduced from ref. 81 with permission from the American Chemical Society. (C) Unconventional L- and inverse-L shaped pillar arrays for sorting and biophysical measurement of immune cell population from whole blood directly. Reproduced from ref. 83 with permission from Wiley. (D) Capillary-driven based DLD platform to isolate MCF-7 from RBCs. Reproduced from ref. 86 with permission from Royal Society of Chemistry. (E) A two-stage cascaded DLD platform for isolating *E. coli* from whole blood. Reproduced from ref. 84 with permission from Nature Research. (F) NanoDLD arrays on a silicon–glass microfluidic chip to separate EVs from serum samples. Reproduced from ref. 77 with permission from the Royal Society of Chemistry.

labeling,[51,56] high cost (*e.g.* antibodies),[1] and sorting performance being dependent on the operators.[53] The current gold standard for EV isolation is differential ultracentrifugation (UC),[57] which is not suitable for clinical testing as it is time-consuming (~4–5 h) and prone to EV losses.[58] Other commercial approaches such as immunoaffinity might affect EV functionality[59] or result in high protein contamination.[60] Size-exclusion chromatography (SEC), which achieves size-based EV separation through a resin column, has been gaining traction in recent years.[61,62] A common issue for the aforementioned EV isolation methods is that they all require pre-processed blood (plasma)

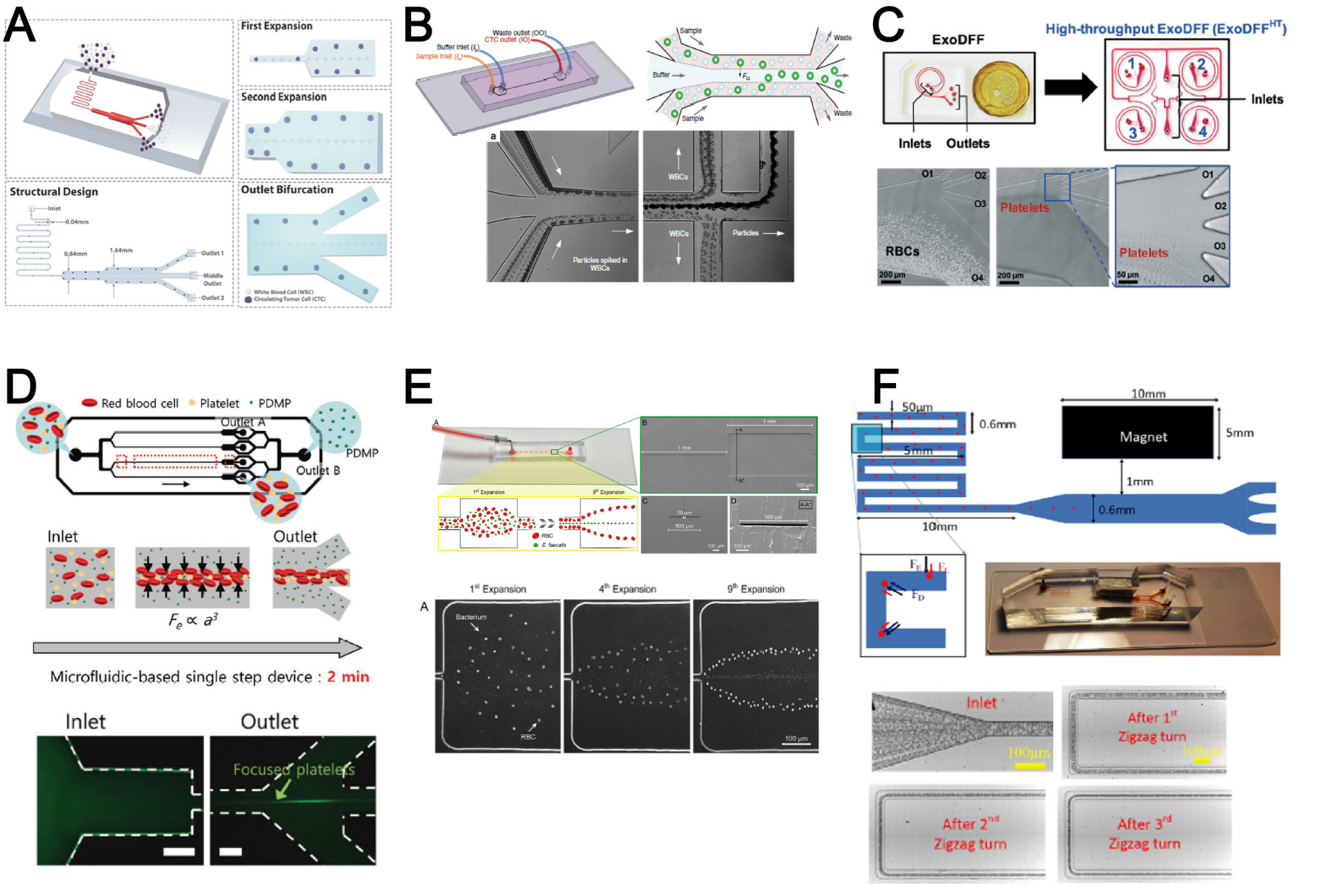

Fig. 4 Inertial microfluidics and viscoelastic focusing for blood separation. (A) Illustration of cell distribution positions and force analysis in a zigzag structured with a straight expansion channel based inertial microfluidic chip. Reproduced from ref. 93 with permission from the American Chemical Society. (B) Size-based differential migration of cells towards buffer flow in the middle of the main channel. Reproduced from ref. 94 with permission from Springer Nature. (C) Images of a spiral shaped single and multiplexed ExoDFF device for isolation of circulating EVs. Reproduced from ref. 97 with permission from the Royal Society of Chemistry. (D) Schematic illustration of platelet-derived micro-particle (PDMP) separation in a straight microfluidic device using viscoelastic non-Newtonian fluid. Reproduced from ref. 100 with permission from Wiley. (E) Schematic representation of red blood cell and bacteria sorting in a cascaded contraction–expansion microchannels. Reproduced from ref. 101 with permission from Elsevier. (F) Illustration of particle migration at the U-turn zigzag channel. Reproduced from ref. 103 with permission from Wiley.

as the starting sample, which itself involves several manual centrifugation steps. In this section, we will discuss recent progress in microfluidic label-free sorting of different blood cellular constituents using active (acoustophoresis, dielectrophoresis) and passive (viscoelastic, inertial focusing, deterministic lateral displacement (DLD), filtration, biomimetic cell margination) methods (Fig. 1). The representative microfluidic techniques based on different cell types for blood fractionation and their performance metrics are summarized in Tables 1–3.

Filtration

Microfluidic filtration separate cells based on size and can be broadly divided into three categories: membrane filtration,[63,64] pillar filtration,[65] and tangential flow filtration.[66] While readers are highly encouraged to learn more about the various filtration mechanisms from other excellent review articles,[45,67,68] this section focuses on their applications to isolate CTCs,[63–65,69] leukocytes,[70] platelets,[66,71] bacteria,[72] and EVs[73–75] from whole blood. In general, key advantages of filtration methods include scalable throughput, low-cost and simple operation. However, most blood filtration devices are affected by clogging and bubble formation issues that may affect the sorting efficacy. Selection of membrane size cut-off and flow parameters is also an important consideration as larger cells may be trapped or deform through pores under high pressure which results in lower cell recovery.

Membrane filtration generally uses commercial membranes with through holes to trap or isolate larger cells. Kang *et al.*[64] improved the membrane with unique tapered-slits to increase the sample throughput for CTC isolation (Fig. 2A). This tapered-slit filter fabricated with a photosensitive polymer was connected to a syringe to achieve a high CTC capture rate of 77.7% and viability of 80.6%. Besides single CTC isolation, Sarioglu *et al.*[65] developed a cluster-chip based on pillar filtration to isolate CTC clusters from whole blood directly (Fig. 2B). A set of triangular pillars were designed to capture CTC clusters which successfully

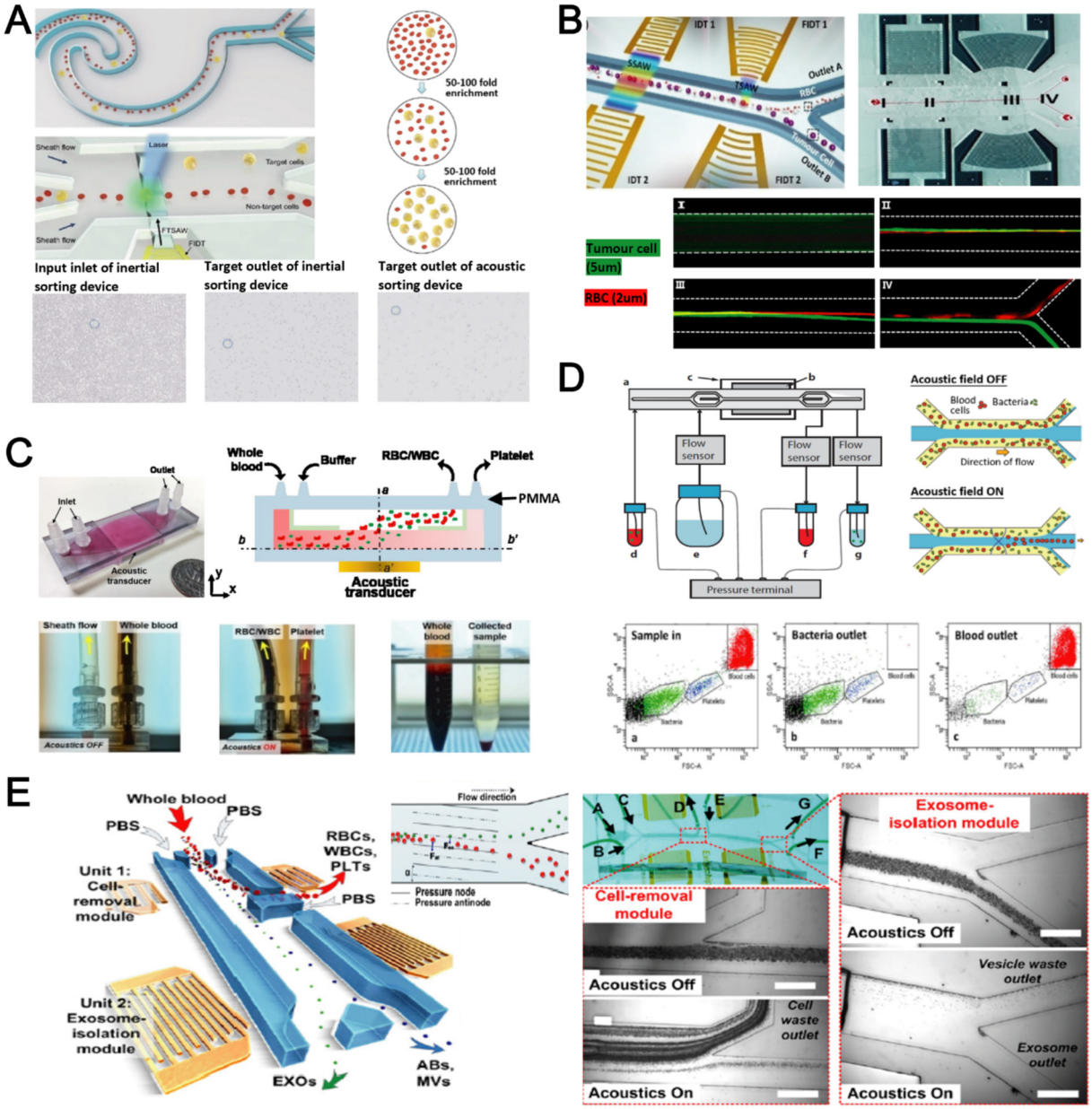

Fig. 5 Acoustofluidics based blood fractionation. (A) CTC isolation and enrichment using a hybrid (inertia and acoustic) microfluidic sorting device. Reproduced from ref. 108 with permission from the Royal Society of Chemistry. (B) Tumour cells isolated by a multi-stage surface acoustic wave (SAW) device. Reproduced from ref. 109 with permission from Elsevier. (C) Platelet isolation using a PMMA plastic-based device. Reproduced from ref. 113 with permission from the Royal Society of Chemistry. (D) Clinical-scale automated isolation of bacteria. Reproduced from ref. 115 with permission from Nature Research. (E) Exosome isolation by taSSAW (tilted-angle standing SAW) using a dual-stage acoustofluidic device. Reproduced from ref. 117 with permission from United States National Academy of Sciences.

identified CTC clusters in 30–40% of patients with metastatic breast or prostate cancer or with melanoma. Another pillar-based device was used for continuous separation of platelets from whole blood in a radial sample flow direction (Fig. 2C).[66] The multiple radial parallel paths and self-generating cross flow greatly minimize clogging to achieve a ~60× platelet enrichment.

Another form of filtration is tangential flow filtration, also commonly known as cross-flow filtration. In this approach, the sample will flow close and parallel ("pinched") to the filtration structure using an additional sheath flow, while a pressure gradient is established to promote cells passing through small gaps perpendicular to the flow direction. Han *et al.*[75] fabricated a microfluidic chip by bonding two polymethyl methacrylate (PMMA) layers with a nanoporous membrane to isolate and purify exosomes from human blood with a higher recovery rate (>80%) (Fig. 2D). Raub *et al.*[72] designed a microfluidic device using cross-flow filtration for separation of bacteria from blood cells (Fig. 2E). This chip could remove 97–98% of RBCs and retain 30% of bacteria

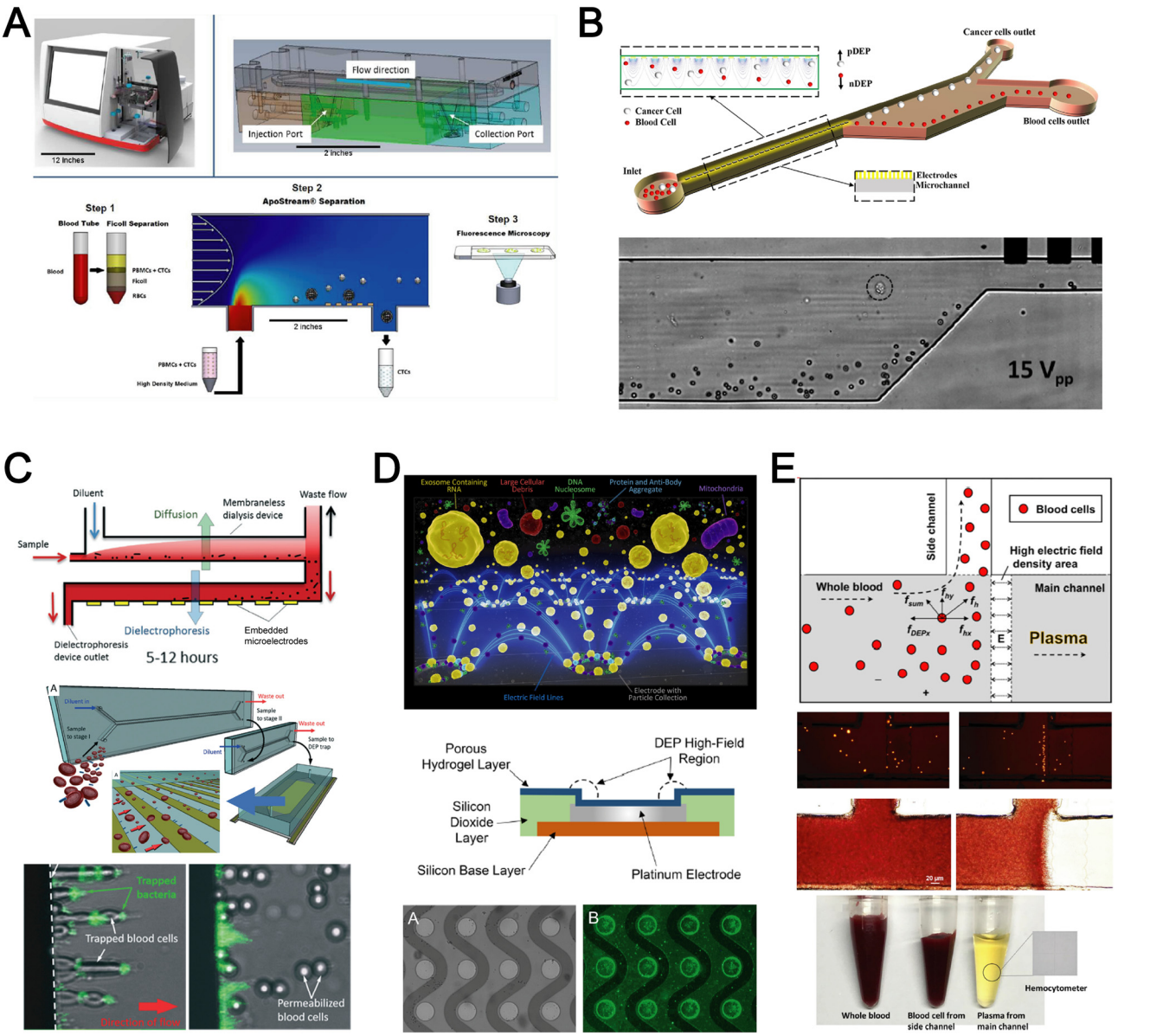

Fig. 6 Dielectrophoresis (DEP) based blood fractionation. (A) ApoStream® system for separating CTCs from peripheral blood mononuclear cells (PBMCs) under continuous flow. Reproduced from ref. 121 with permission from Public Library of Science. (B) Continuous sorting of human breast cancer cells from blood cells in low conductivity sucrose–dextrose medium. Reproduced from ref. 122 with permission from Wiley. (C) Combined microdialysis and DEP for bacterial isolation from blood. Reproduced from ref. 125 with permission from the Royal Society of Chemistry. (D) Rapid exosome isolation from whole blood using an alternating current electrokinetic (ACE) microarray. Reproduced from ref. 128 with permission from the American Chemical Society. (E) Continuous cell-free plasma extraction from undiluted blood. Reproduced from ref. 131 with permission from Wiley.

from undiluted whole blood with a higher relative bacterial abundance of 8200%. A new hydrodynamic filtration multiplexed method was reported to separate leukocytes from diluted blood samples at an ultra-high throughput of 15 mL min^{-1} and a leukocyte recovery ratio of ~94% (Fig. 2F).[70]

Deterministic lateral displacement (DLD)

Deterministic lateral displacement (DLD) is an established microscale separation technique that uses an array of micropillars to displace larger particles laterally[76] in a bumping migratory flow trajectory.[76–78] By carefully designing the critical sorting diameter (D_c) based on the formula: $D_c = 1.4Ge^{0.48}$, where G is the spacing between pillars and e is the row shift fraction ($e = \tan q$) when q is the tilt angle,[79,80] DLD can be exploited for blood processing to separate CTCs,[81–83] leukocytes,[84] bacteria[77] and EVs (Fig. 3).[77] Since the first DLD work reported in 2004,[85] many research groups have explored different sorting applications and improved the technique in terms of scalability and separation resolution with different pillar designs. Recent advances in blood fractionation include the use of a novel cascaded DLD approach to isolate CTC

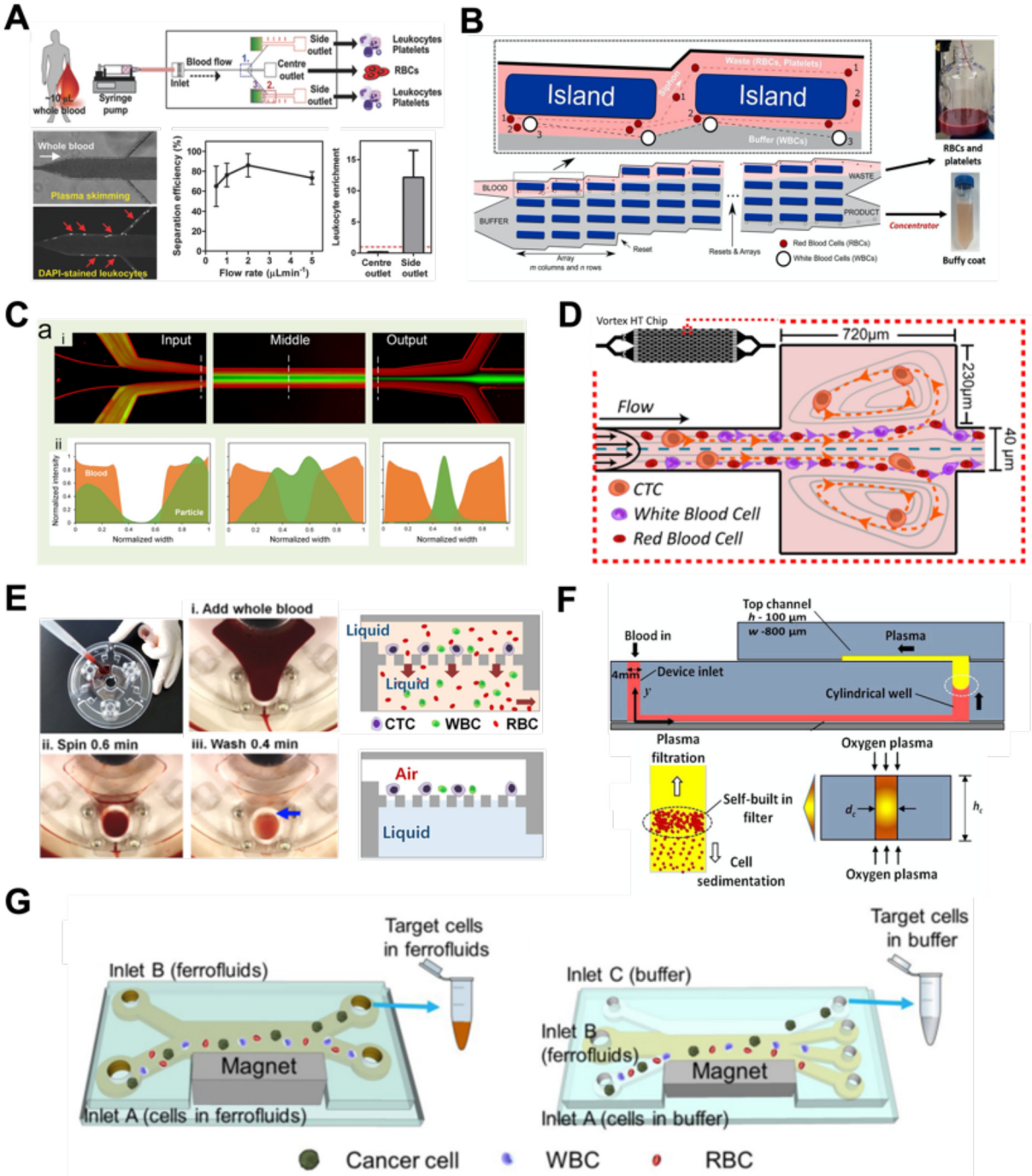

Fig. 7 Other label-free fractionation methods. (A) Isolation of WBCs from a drop of blood using the biomimetic cell margination effect. Reproduced from ref. 5 with permission from Wiley. (B) Non-equilibrium inertial separation array (NISA) for isolation of WBCs from whole blood by passive inertial lift forces exerted by an island array. Reproduced from ref. 133 with permission from Nature Research. (C) Shear-induced diffusion (SID) used to separate 18.7 μm fluorescent particles (green) from 2× diluted whole blood (red). (i) Overlapped pseudocolored images indicating a high-efficiency separation; (ii) corresponding intensity profiles across the dashed lines in part (i). Reproduced from ref. 134 with permission from Springer Nature. (D) High Throughput Vortex Chip (Vortex HT) that traps larger cells in microvortices developed in reservoirs, while allowing smaller cells to pass through to achieve separation. Reproduced from ref. 137 with permission from Impact Journals. (E) Lab-on-a-disc system equipped with fluid-assisted separation technology (FAST) for CTC isolation from whole blood. Reproduced from ref. 152 with permission from the American Chemical Society. (F) Microfluidic device using a combination of capillary flow, differential wetting and sedimentation effects for the separation of plasma. Reproduced from ref. 142 with permission from Nature Research. (G) Negative magnetophoresis separation of cancer cells using ferrofluid. Reproduced from ref. 145 with permission from Royal Society of Chemistry.

clusters from whole blood with a recovery yield of 91.8% and 48% for large and small CTC clusters, respectively.[79] In contrast to conventional single-stage DLD devices, Au *et al.* integrated asymmetrical pillars and channel height

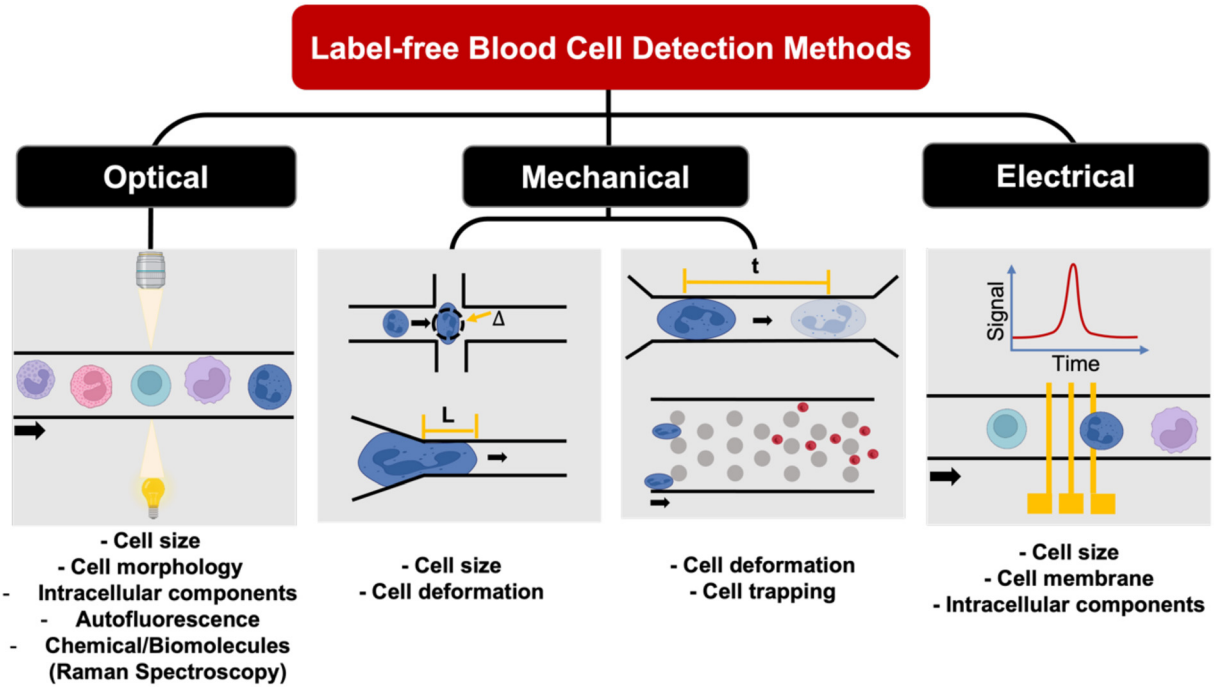

Fig. 8 Overview of microfluidic label-free single cell analysis.

restriction in a dual-stage DLD chip to achieve high CTC yield and integrity with a lower shear stress rate (Fig. 3A).[79] Besides particle separation, efforts have also been made to incorporate different functionalities in DLD systems. An example is the integration of a droplet generator with DLD to encapsulate single DLD-purified leukocytes in droplets for protease analysis (Fig. 3B).[81] Another work demonstrated the application of a label-free and rapid (15 min) combinational DLD assay to measure the biophysical properties (cell deformability) of immune cell population from 20 mL of whole blood for point-of-care testing (Fig. 3C).[83] These measurements were correlated to patient clusters with different levels of immune severity, thus facilitating early detection of asymptomatic-infected individuals before the condition exacerbates into sepsis.

To improve portability, a capillary paper pump-based DLD method was recently reported to isolate MCF-7 breast cancer cells (>90% viability) from RBCs (Fig. 3D).[86] The capillary pumps rely on a negative pressure imposed by the downstream capillary action to initiate fluid flow over a prewetted or hydrophilic DLD array surface. Finally, researchers have also successfully scaled down the DLD cell sorting technique for smaller (sub-micron) bacteria and EV isolation.[77,84] One study highlighted *E. coli* isolation from whole blood using a two-stage cascaded DLD approach to achieve a recovery yield of 25–50% (Fig. 3E).[84] Smith *et al.* also reported a microfluidic silicon–glass nanoDLD array to selectively enrich large EVs from serum using a pillar gap distance of 225 nm. This resulted in the highest yield of ~50% with a significantly shorter processing time (60 min) as compared to ultracentrifugation (Fig. 3F).[77] While DLD is a highly versatile size-based blood separation technique, it should be noted that the sorting performance can be influenced by other factors including particle shape and deformability, and the presence of cell aggregates.[76] Clogging issues and non-specific cell binding must be minimized during blood processing which can otherwise directly impact cell movements within the pillar array.

Inertial microfluidics

Inertial microfluidics is a hydrodynamic cell focusing method based on the interplay between inertial lift forces and Dean drag forces acting on particles under Newtonian flow. Several review articles have recently discussed the fundamentals and applications of inertial microfluidics.[87–89] As these forces are particle size dependent, different cells are focused on distinct equilibrium positions to achieve continuous and high throughput (~mL min^{-1}) cell separation for different bio-fluids including blood, urine,[90] and semen samples.[91] When designing inertial cell sorters, it is important to consider both target and non-target cell sizes, starting sample concentration and volume, fluid properties, and channel dimensions for optimum focusing.[92]

Abdulla *et al.* reported a zigzag microchannel for label-free separation of CTCs from whole blood.[93] The zigzag structure was used to promote size-based particle migration and help stabilize the focused particles and larger CTCs (>10 μm) to the channel center (Fig. 4A). Zhou *et al.* used a multi-flow straight microfluidic device to demonstrate the separation of CTCs directly from whole blood (Fig. 4B). Using a 2-inlet system, the larger CTCs migrated to the channel center into a clean buffer flow with a high purity (>87%) and recovery (>93%) rate.[94]

Table 1 Comparison of microfluidic label-free blood fractionation for immune cells and CTCs

Principles	Sample type	Throughput	Efficiency/recovery	Purity/sensitivity/enrichment	Ref.
Filtration	Spiked blood	10 mL h^{-1}	>90% recovery	N.A.	63
	Diluted blood	10 mL h^{-1}	77.7% efficiency	17.44% purity	64
	Whole blood	2.5 mL h^{-1}	99% efficiency	N.A.	65
	Spiked blood	1 mL h^{-1}	95% efficiency	99% purity	69
	Whole blood	37.5 μL min^{-1}	72.1% recovery	15.1% purity 232-Fold enrichment	236
	Diluted blood	40 μL min^{-1}	N.A.	78 ± 14% purity	237
	Diluted blood	1 mL min^{-1}	~94% efficiency	~4000-Fold enrichment	70
DLD	Whole blood	0.5 mL h^{-1}	~91.8% recovery for large CTC clusters ~48% recovery for small CTC clusters	N.A.	79
	Whole blood	10 μL min^{-1}	~80% recovery	N.A.	81
	Whole blood	10 000 cells per s	N.A.	0.91 sensitivity	83
	Spiked RBC	110 s 100 mL^{-1}	95% recovery	N.A.	86
Inertial microfluidics	Whole blood	720 μL min^{-1}	88.1% efficiency	N.A.	95
	Whole blood	0.4 mL min^{-1}	>80% efficiency	N.A.	93
	Whole blood	80 mL h^{-1}	90% recovery	N.A.	238
Viscoelastic focusing	Whole blood	200 μL min^{-1}	67% recovery	N.A.	100
	Whole blood	12 μL min^{-1}	98% efficiency	N.A.	101
	Whole blood	30 μL h^{-1}	76% efficiency	N.A.	102
DEP	Lysed blood	0.4 μL min^{-1}	N.A.	N.A.	124
	PBMCs	35 μL min^{-1}	53–70% efficiency	N.A.	121
	Spiked blood	6 μL h^{-1}	100% recovery	81% purity	122
	PBMC	4–7 μL h^{-1}	N.A.	N.A.	123
Acoustophoresis	Diluted blood	1.0 μL min^{-1}	N.A.	2500-Fold enrichment	108
	Spiked phosphate buffer solution	0.3 μL min^{-1}	90% ± 2.4% efficiency	N.A.	109
	Lysed blood	6 mL h^{-1}	91.8 ± 1.0% efficiency for breast CTCs 84.1 ± 2.1% efficiency for prostate CTCs	20-Fold enrichment for breast CTCs 20-Fold enrichment for prostate CTCs	110
	Lysed blood	2.5 mL h^{-1}	87% recovery	0.11% purity 162-Fold enrichment	111
	Lysed blood	100 μL min^{-1}	85.0% efficiency for prostate CTCs 89.8% efficiency for breast CTCs	53 ± 27-fold enrichment for prostate CTCs 84 ± 30-fold enrichment for prostate CTCs	112
	Lysed blood	7.5 mL h^{-1}	86% efficiency	N.A.	239
Others	Diluted blood	3 mL min^{-1}	96.6% efficiency	N.A.	133
	Whole blood	0.5–5 μL min^{-1}	>80% efficiency	12-Fold enrichment	5
	Whole blood	3 mL min^{-1}	95.9 ± 3.1% recovery	N.A.	152
	Whole blood	6.75 mL h^{-1}	89.8% efficiency	N.A.	134
	Diluted blood	800 μL min^{-1}	83% efficiency	N.A.	174
	WBCs	1.2 mL h^{-1}	82.2% efficiency	N.A.	145

Spiral inertial microfluidics is another popular cell sorting design due to its larger channel dimensions which minimizes clogging issues during blood processing. Zhu *et al.* reported a novel inertial microfluidic (IM) cube which was integrated with four subunits of spiral channels and stacked in multiple layers to extract WBCs from 1.3 mL of whole blood within 2 min.[95] The design is based on passive secondary flow mixing and inertial sorting to achieve complete RBC lysis and a white blood cell extraction efficiency of 88.1%.

A major bottleneck in inertial microfluidics is the inability to separate small particles as they experience insufficient inertial forces, or require excessively long channel lengths to migrate to their equilibrium positions (large pressure drop). To address this issue, Tay *et al.* reported a novel transient (non-equilibrium) cell focusing method in spiral channels based on subtle differences in the particle innermost distance (D_{inner}) from the channel inner wall to separate sub-micron bacteria and nanoparticles.[96] This was subsequently adapted to isolate EVs from whole blood directly (ExoDFF) and multiplexed to process 5 mL of whole blood within an hour with the same EV separation performance (Fig. 4C).[97]

Viscoelastic focusing

Another passive microfluidic cell sorting method gaining in popularity is using viscoelastic focusing effects. Briefly, the

Table 2 Comparison of microfluidic label-free blood fractionation based on platelets, bacteria and plasma

Principles	Sample type	Throughput	Efficiency/recovery	Purity/sensitivity/enrichment	Ref.
Filtration	Whole blood	1 mL min^{-1}	>80% recovery	N.A.	71
	Whole blood	600 nL min^{-1}	97% recovery	~70% purity 60-Fold enrichment	66
	Whole blood	100 ± 30 mL min^{-1}	30% efficiency	N.A.	72
DLD	Spiked blood	DLD1: 100–600 μL min^{-1}	DLD1: 50% recovery	N.A.	84
		DLD2: 7–50 μL min^{-1}	DLD2: 25% recovery		
DEP	1000× diluted plasma	2 μL, 2 min	N.A.	N.A.	127
	Whole blood	10 μL min^{-1}	~78% efficiency	N.A.	125
	20× diluted blood	18 μL h^{-1}	97% efficiency	N.A.	126
Viscoelastic focusing	Whole blood	10–32 μL min^{-1}	N.A.	N.A.	103
Acoustophoresis	Undiluted whole blood	20 mL min^{-1}	87.3% efficiency	82.9% purity	240
	Whole blood	1.5 μL min^{-1}	86% efficiency	7.7-Fold enrichment	114
	Undiluted whole blood	10 mL min^{-1}	>85% efficiency	N.A.	241
	Diluted whole blood	80 μL min^{-1}	90% efficiency	103-Fold enrichment	242
	Culture media	5 mL min^{-1}	N.A.	N.A.	116
Others	Whole blood	0.66 μL min^{-1}	N.A.	99.9% purity	142
	Whole blood	1.5 min for plasma, 15 min for buffy coat	N.A.	100% purity	141

Table 3 Comparison of microfluidic label-free blood fractionation based on EVs

Principles	Sample type	Throughput	Efficiency/recovery	Purity/sensitivity/enrichment	Ref.
Filtration	Diluted plasma	50 μL min^{-1}	>97% efficiency >80% recovery	N.A.	75
	Undiluted serum	90 μL min^{-1}	N.A.	N.A.	73
	Plasma	5–10 μL min^{-1}	N.A.	N.A.	74
DLD	Serum	900 μL h^{-1}	~70% recovery	2.6–3.0-Fold enrichment	77
Inertial microfluidics	Whole blood	80 μL min^{-1}	~15% efficiency	N.A.	97
Viscoelastic focusing	Adenocarcinoma human alveolar Basal epithelial cells	200 μL h^{-1}	>80% recovery	>90% purity	99
DEP	Culture media	1.5 μL min^{-1}	81% recovery	95% purity	130
	Plasma	3–5 μL min^{-1}	N.A.	N.A.	128
Acoustophoresis	Plasma	0.5 μL min^{-1}	N.A.	N.A.	243
	Undiluted whole blood	4 μL min^{-1}	82.4% efficiency	98.4% purity	244

elasticity of dilute polymer solutions causes the lateral migration of single particles to focus on the channel center due to a non-uniform distribution of the normal stress between the centerline and the walls of the microchannel.[98] Besides optimizing flow rates or channel dimensions, one can also tune the concentration of the polymer (poly(ethylene oxide), PEO) to control viscoelastic forces and particle separation resolution at lower flow rates. Liu *et al.* reported a straight microchannel design to separate exosomes from other larger EVs with high separation purity (>90%) and recovery (>80%) by adding a small amount of PEO (0.1 wt%) into the cell culture medium.[99]

Recently, a sheathless focusing device using viscoelastic fluid was reported to isolate platelet-derived micro-particles (PDMPs ~ 0.3–2 μm) from RBCs with a 4.8-fold increase in yield as compared to the centrifugation within 2 min (Fig. 4D).[100] Similarly, Bilican *et al.* also developed a cascaded expanding-contracting straight microchannel for sheathless separation of *Enterococcus faecalis* (~0.5–2 μm) in viscoelastic fluid with 98% separation efficiency (Fig. 4E).[101] As single inlet devices are simple to operate, there are several other interesting sheathless cell sorting devices using viscoelastic focusing to achieve undiluted whole blood separation,[102] integration with positive magnetophoresis (Fig. 4F),[103] and a scaled-up double spiral design.[104]

Although both inertial and viscoelastic focusing microfluidic technologies are useful for separating nano to microscale particles from blood, there are still challenges to improve the separation dynamic range in a single chip for complete blood fractionation. The use of viscoelastic or polymer solution can enhance cell focusing but may affect downstream analysis (*e.g.* mass spectrometry) with additional chemical components or rare cell isolation. Future studies are warranted to investigate cell biocompatibility and

functionalities after prolonged exposures (~days). More details on viscoelastic microfluidic mechanisms and applications can be found in a review by Papautsky *et al.*[105]

Acoustophoresis

Acoustophoresis (or acoustofluidics) is an active method which uses an external acoustics field to manipulate particles. In general, microfluidic devices consist of interdigitated transducers (IDTs) using a piezoelectric material to generate bulk acoustic waves (BAWs) and surface acoustic waves (SAWs). This leads to the formation of pressure and anti-pressure nodes for size or density-based particle separation in a contactless and label-free manner.[106,107] With recent advances in improving biocompatibility, cascaded designs, multiplexed cell sorting and scalable manufacturing, acoustofluidic technologies have demonstrated their potential for point-of-care blood-based clinical applications.

Using a hybrid platform, Zhou *et al.* combined passive (inertia sorting) and active (acoustic sorting) methods to isolate CTCs from 10× diluted whole blood (Fig. 5A).[108] The first section consists of a reverse 'S'-curved microchannel design to deplete RBCs while focusing the larger CTCs to the acoustic sorter to sort fluorescence-labelled MCF-7 cells. In another work, Wang *et al.* utilized a pair of IDTs to generate standing SAWs (SSAW) to focus CTCs and RBCs on a single pressure node at the channel centre. Next, larger particles (>5 μm) would be deflected laterally due to the larger acoustic radiation induced by travelling pulsed SAWs (TSAW).[109] The authors applied this to sort U87 glioma cells from the RBCs without the need for sample dilution (Fig. 5B). Similar CTC acoustic sorting devices were also reported by other groups with improved throughput[110,111] or combined with negative selection of WBCs.[112]

Key advantages of acoustofluidic platforms include the tunability of the acoustics field strength for smaller particles and scalability for large sample volume processing. For example, Gu *et al.* isolated platelets (2–3 μm) using a PMMA disposable device which is suitable for rapid fabrication and clinical use (Fig. 5C).[113] By producing a pressure node near the top layer with a quarter-wavelength resonator, blood cells were deflected vertically to the top layer to achieve a platelet recovery rate of 87.3% at an ultra-high throughput of 20 mL min^{-1}. Another scaled up platelet separation device fabricated by the lithography method was reported using SSAW.[114] Besides platelets, bacterial separation (>90% recovery) from whole blood is also reported based on bulk acoustophoresis (Fig. 5D).[115] Another work was reported by Devendran *et al.* to separate bacteria at 5 mL min^{-1} by utilizing diffractive-acoustic SAW (DASAW) to focus particles along a 90-degree angled serpentine channel with only a single travelling wave.[116]

For sub-micron particles, Wu *et al.* developed a dual-modular acoustofluidic platform with a microscale cell-removal module followed by an nanoscale exosome isolation module.[117] Both sections use tilted-angle standing SAW (taSSAW) fields to filter out blood components larger than 1 μm (>99.9% blood cell removal) in the first stage, and a higher frequency of 40 MHz to separate EVs and apoptotic bodies with a purity rate of 98.4% at the 2nd stage (Fig. 5E). Taken together, acoustics-based sorters are scalable, versatile and have excellent sorting performances. Due to frequent bubble formation and high setup costs, future work will focus on improving the device robustness and their translation for clinical use.

Dielectrophoresis

Dielectrophoresis (DEP) is another established active label-free cell sorting method based on electrical properties of particles and medium. Under a non-uniform electric field, particles or cells are polarised and a net dipole moment is induced on particles' surfaces, thereby allowing them to migrate along or against the electric field depending on the excitation frequency, particle size, and electrode configuration.[118] In most devices, the electrodes are orientated to exert DEP forces perpendicular to the flow direction for lateral particle sorting into different channel outlets.[119,120]

For DEP-based cell sorting, it is often combined with flow fractionation to take advantage of the parabolic velocity profile and laminar flow in microchannels. The ApoStream® system is a commercial product that separates CTCs from peripheral blood mononuclear cells (PBMCs) using DEP-based flow fractionation (Fig. 6A).[121] Briefly, CTCs introduced at the channel bottom experienced stronger DEP forces towards the bottom outlet while smaller PBMCs are repelled vertically to the channel center (faster flow) and eluted as waste. Similarly, Alazzam *et al.* applied lateral DEP to separate MDA-MB-231 cancer cells from blood cells with 100% recovery and 81% purity (Fig. 6B) using a low conductivity sucrose–dextrose medium.[122] To enhance CTC sorting, Dudaie *et al.* integrated DEP with image-based CTC discrimination using interferometric phase microscopy to achieve 98% classification success and 69% sorting accuracy.[123] Besides sorting, DEP can also be applied for leukocyte activation profiling in a sepsis murine model since activated leukocytes are larger in size and thus experience stronger DEP forces to deflect to different channel positions.[124]

Instead of DEP-induced particle lateral deflection under continuous flow, smaller bacteria and exosomes can be attracted and trapped at the electrodes by DEP forces to facilitate detection. D'Amico *et al.* combined microdialysis and dielectrophoresis to deplete permeabilized red blood cells before trapping bacteria on electrodes to achieve ~79% separation efficiency using spiked blood samples (10^3–10^5 CFU mL^{-1}) (Fig. 6C).[125] Numerous DEP studies also reported higher bacteria separation efficiency[126] or detection limit[127] using diluted blood or plasma. For exosome isolation, Ibsen *et al.* reported a rapid EV isolation using an alternating

current electrokinetic (ACE) microarray from 50 μL of undiluted blood, followed by on-chip immunofluorescence detection of EV proteins within 30 min (Fig. 6D).[128] It was further used to distinguish pancreatic ductal adenocarcinoma patients from healthy subjects with 99% sensitivity and 82% specificity.[129] Submicron particle separation was also demonstrated using combined DEP with acoustophoresis to separate exosomes (<200 nm) from microvesicles (>300 nm) in culture media with 95% purity and 81% recovery.[130] Yang *et al.* reported a microfluidic DEP device for direct plasma extraction from undiluted blood which can be automated to replace conventional centrifugation (Fig. 6E).[131]

Overall, DEP is a tunable blood fractionation method and can complement passive size-based sorting methods to fractionate cells of similar sizes but different electrical properties. However, issues including Joule heating, limited throughput, and the need for a low conductivity buffer need to be addressed to facilitate the translation of DEP technologies for clinical testing.[132]

Other label-free blood fractionation methods

Aside from the aforementioned techniques, several non-conventional methods have also been reported for blood sorting applications. Tay *et al.* reported a microfluidic device to separate WBCs from undiluted whole blood based on the effect of biomimetic cell margination (Fig. 7A), a microcirculatory phenomenon whereby deformable RBCs migrate laterally toward the axial centre (Fahraeus effect) and result in an RBC-free layer (containing WBCs) at the vessel periphery.[5] In another work, Mutlu *et al.* devised a non-equilibrium inertial separation array (NISA) that utilizes inertial lift forces to separate WBCs from blood. Unlike DLD, NISA adopts longer rectangular islands that use size-dependent inertial lift forces to push cells away from channel walls (Fig. 7B).[133] The authors reported a sample throughput of ~3 mL min^{-1} with 96.6% WBCs yield and 0.0059% RBC contamination, making NISA suitable for large blood volume processing applications such as banked blood cleansing and rare cell enrichment.

Another interesting label-free blood separation technique is shear-induced diffusion (SID), used for isolating CTCs[94,134] and leukocytes[135] from whole blood. The set-up involves a sandwiched buffer solution co-flowed with two sample streams, where target cells migrate from the side into the cell-free central stream under the influence of shear-induced diffusion and inertial forces. While the underlying mechanism of SID has yet to be fully elucidated,[135] larger cells (WBCs, CTCs) in the blood samples are observed to migrate into the buffer stream faster than smaller cells (RBCs) due to size-dependency of SID and inertial forces.[134] This size-based migration and focusing has also been attributed to the downstream velocity of particles,[135] which scales inversely with particle size. Using this strategy, Zhou *et al.* demonstrated the separation of beads (18.7 μm) and HepG2 cancer cells from whole blood at a high throughput of 6.75 mL h^{-1} (10^6–10^7 cells per s) and an efficiency of 89.8% (Fig. 7C).[134] As a proof-of-concept, the authors also applied SID for the isolation of CTCs from hepatocarcinoma subjects. While they were able to detect one CTC from 1 mL of blood *via* immunostaining, the purity of the sorted samples was affected by large WBCs. A low shear rate at the flow interface must be carefully maintained to minimize RBC diffusion.[136] Nevertheless, the ability of SID to process highly concentrated samples and achieve higher throughput than typical inertial microfluidics shows great potential as a label-free cell isolation method. For CTC isolation, several studies have reported the use of microvortices to trap CTCs by designing a series of narrow channels with expanded reservoirs.[137–140] Rapid flow in the narrow channel generates inertial forces to trap larger cells into the vortices in the reservoirs while smaller cells are allowed to pass through. After separation, the trapped CTCs can be "released" from the reservoirs using a slower flow rate and eluted into a small volume for off-chip processing. Using this phenomenon, Che *et al.* developed and clinically validated a high throughput vortex chip for size-based CTC enrichment with a capture efficiency of 83% at a throughput of 800 μL min^{-1} of whole blood (Fig. 7D).[137] In a study by Dhar *et al.*, they integrated vortex trapping of CTCs with single-cell encapsulation in a single platform termed SPEC (size-based purification and encapsulation of cells) by using the reservoirs as mini reaction chambers for the downstream study of rare cell secretion at the single-cell level.[138]

Using a different strategy, Kim *et al.* reported a lab-on-a-disc platform with an integrated fluid-assisted separation technology (FAST) to selectively capture CTCs on the polyethylene membrane filter (8 μm pore size) based on centrifugal effects. The novelty of this technique is the addition of a stably-held liquid throughout the size-based CTC isolation process, which reduced clogging and increased the recovery rate significantly from 54.0 ± 21.0% to 95.9 ± 3.1% (Fig. 7E). Another interesting work based on centrifugal force is the development of an ultra low-cost (<20 cents), human-powered paper centrifuge inspired by a whirligig toy, aptly termed 'paperfuge'.[141] A high rotational speed of 125 000 r.p.m. (~30 000 g) was reported which can separate plasma from whole blood in <1.5 min when blood-filled capillary tubes are mounted on the discs. By modifying channel surface properties, Maria *et al.* proposed a capillary flow-driven, double layered PDMS device with a wettability gradient for plasma extraction (Fig. 7F).[142] As blood enters the bottom microchannel *via* capillary action and moves up the vertical well, the hydrophobic region enhances plasma separation by exploiting the velocity differences between plasma and cells. Combined with sedimentation effects, 2 μL of plasma was extracted from <10 μL whole blood in 15 min for blood glucose measurements.

Lastly, while magnetic isolation is typically affinity-based using antibodies, an interesting label-free approach is

negative magnetophoresis using ferrofluids.[143–146] Ferrofluids are stable colloid suspensions of ferromagnetic nanoparticles such as magnetite or maghemite[147] dispersed in a non-magnetic carrier fluid such as water or organic solvent.[148] Cells and particles suspended in ferrofluids behave as "magnetic voids"[149] which are deflected to distinct size-based flow trajectories when an external magnetic field is applied to attract magnetic nanoparticles.[145,150] As most commercial ferrofluids are not biocompatible,[143] careful selection of the ferrofluid material, pH and surfactant is crucial for cell manipulation.[147] Zhao *et al.*[145] developed a biocompatible approach using a ferrofluid to isolate cancer cells at low concentrations (~100 cells per mL) from WBCs at a throughput of 1.2 mL h^{-1} and an average efficiency of 82.2% (Fig. 7G). A custom-made biocompatible ferrofluid flow is flanked by two buffer streams, and the blood sample is introduced through one of the buffer inlets. An external magnetic force pushes the target cancer cells into the opposite buffer flow, thereby minimizing the residency time in the ferrofluid stream and increasing the cell viability (94.4 ± 1.3%) when tested with 7 cancer cell lines. It should be noted that the adoption of ferrofluids for cell separation is limited by hindrance in optical imaging due to light diffraction of ferrofluids.[148,151] Hence, the nanoscopic properties of ferrofluids have to be further optimized to develop new bio-applications.

Label-free single cell analysis

Unlike conventional biological assays which provide average (bulk) readout, single cell analysis of a large cell population is a powerful method to probe cell heterogeneity. Label-free single cell analysis enabled by microfluidics offers alluring prospects including minimal sample preparation time, cost-effectivity and usefulness in diseases with no known biomarkers. These approaches mostly analyze intrinsic cellular properties such as cell morphology, spectrochemical properties, dielectric parameters and mechanical characteristics for non-invasive liquid biopsy[153] and point-of-care diagnostics.[154] Herein, we summarize recent innovations

Table 4 Microfluidic label-free single cell analysis based on different principles

Method	Sample type	Key results	Ref.
Optical properties			
Digital holographic microscopy	Plasma	Discriminate healthy and pathological samples; classify leukemias	159
QPI (quantitative phase imaging) flow cytometry	Culture medium	Ultra high-throughput (>10 000 leukemic cells per s); flow (2.3 m s^{-1})	245
Fluorescence lifetime imaging microscopy (FLIM)	Diluted whole blood	Combination of single-cell trapping array separation with real-time FLIM imaging of leukemia cells	163
Light-scattering	Culture medium	Distinguish and count CD4+ and CD8+ cells (~79% accuracy)	155
Stimulated Raman scattering	Culture medium	Discriminate non-differentiated and differentiated 3T3-L1 cells	168
Stimulated Raman scattering	Whole blood cells, PBMCs, Jurkat cells, HT29 cells	Characterization and classification of cancer cells in blood (~140 cells per s)	169
Optical diffraction tomography	Culture medium	Identification of individual lymphocytes (B, CD4+ T, CD8+ T cells) by 3D-RI tomograms	160
Interferometric plasmonic microscopy	Culture medium	Imaging, sizing, tracking single exosomes	161
Electrical properties			
Impedance cytometry (multi-frequency)	Diluted whole blood	Accurate classification and quantification of 3 subtypes of leukocytes	190
Impedance cytometry (multi-frequency)	Whole blood	Label-free discrimination of platelets, erythrocytes, monocytes, granulocytes and lymphocytes (~3 000 000 cells in 45 min)	193
Impedance cytometry (single-frequency)	Whole blood (RBCs and PBMCs)	Distinguish 1) normal RBCs and GA treated RBCs; and 2) lymphocytes and monocytes (throughput: 20 μL h^{-1})	194
Impedance cytometry (multi-shell model)	Malaria culture	*Plasmodium falciparum* infection characterisation based on membrane capacitance and cytoplasmic conductivity derived from impedance signal	195
Impedance spectroscopy	Whole blood	Isolation of CTCs and WBCs from whole blood, and classification of CTCs and WBCs	197
Impedance spectroscopy	Whole blood	Distinguish sickle red blood cells and normal cells from whole blood using microfluidic chip with oxygen control	199
Mechanical properties			
Optical quantify cell circularity	Blood cells/differentiated blood cells	Plotted mechanical phenotypes for different types of blood cells Showed mechanical properties sensitivity to cytoskeleton change	171
Optical quantify cell geometry	Diluted whole blood	Enriched CTCs from whole blood and performed cell mechano-phenotyping on the same device	174
Optical quantify cell geometrical change during deformation	HL-60	Measured cell Young's modulus and fluidity	177
Electrical quantify cell geometry change	WBCs/HL-60	Used electrical signatures to represent cell geometry and quantified cell geometrical change in a label-free and optics-free setup	178
Electrical quantify cell transit time	CTCs	Used electrical signals to represented cell transition time in constriction channel and characterized cell mechanical properties with transition time	182

on microfluidic label-free blood cell analysis broadly classified as optical imaging, biomechanical analysis, and electrical profiling of single cells (Fig. 8 and Table 4).

Optical properties

Optical detection methods for blood analysis can be based on imaging of cell morphology,[48] or using spectrometry (absorption, scattering),[155,156] surface plasmon resonance,[157,158] refraction[159,160] and interferometric plasmonic microscopy[161] to characterize cellular spectrochemical properties. For whole blood analysis, single cell imaging is typically used for blood cell counting or resolving its size or morphology. Ugele *et al.* reported differential digital holographic (DH) microscopy for native leukocyte detection.[159] The in-flow imaging of a 2D hydrodynamically focused leukocyte stream was performed by using a fixed focal height and moderate depth of field (±2.3 μm) (Fig. 9A). Based on principal component analysis (PCA) of the morphological parameters of the reconstructed images, the differentiation of nine leukocyte subtypes in healthy and pathological samples was achieved. Another interesting work is a high-throughput single leukemic cell imaging platform by utilizing ultrafast quantitative phase imaging (QPI), aptly termed as multiplexed asymmetric-detection time-stretch optical microscopy (multi-ATOM).[162] The multi-ATOM flow cytometer system allows 12-dimensional single-cell biophysical phenotyping at an ultra-large-scale (>1 000 000 cells per s) (Fig. 9B). Such a combination of high throughput and cellular content provides sufficient statistics to distinguish multiple types of leukemia cells from the blood with high accuracy (~92–97%). An integrated platform combining a cell trapping array and phasor-fluorescence lifetime imaging microscopy (phasor-FLIM) for leukemia cell identification was also reported for leukemia cell screening.[163] The array was designed with 1600 packed single-cell traps to filter out RBCs and capture WBC/leukemia cells (Fig. 9C). The trapped single leukemia cells (THP-1, Jurkat and K562 cells) were then distinguished from WBCs in the phasor-FLIM lifetime map as they exhibited significant shift towards shorter fluorescence lifetime. The authors highlighted that this metabolic characterization indicating a higher ratio of free/bound NADH of leukemia cells was due to their stronger glycolysis for rapid proliferation. The identification of T-lymphocyte subclasses (CD4+ and CD8+) by a light scattering approach was recently proposed by Rossi *et al.* (Fig. 9D).[155]

Raman spectroscopy (also commonly termed as Raman flow cytometry) is another powerful optical-based technology which directly probes characteristic intracellular molecular vibrations by measuring the inelastic scattering of incident photons.[164] This is particularly useful to measure metabolites or biomolecules (*e.g.* unsaturated fatty acids, carotenoids and polysaccharides) in live cells which are difficult to detect using fluorescent labelling methods. While spontaneous Raman scattering limits the detection throughput, newer alternatives such as stimulated Raman scattering (SRS) and coherent anti-Stokes Raman scattering (CARS) significantly improve light–sample interaction for high throughput chemical fingerprinting of flowing cells[165,166] or Raman-activated cell sorting.[167] Zhang *et al.* reported a multiplexed SRS flow cytometry platform based on broadband laser excitation and multiplex spectral detection.[168] The system can measure the chemical contents of single particles at high throughput (200 000 spectra per s and 11 000 particles per s) and help discriminate non-differentiated and differentiated 3T3-L1 cells by quantification of different chemical compositions accumulated in single cells (Fig. 9E). A more recent study reported label-free multi-colour SRS microscopy of fast-flowing cells on a 3D acoustic focusing microfluidic device to study cell metabolic heterogeneity in microalgae, blood cells and cancer cells.[169] The setup was based on a fast pulse pair-resolved wavelength-switchable Stokes laser and a galvanometric scanner, achieving a high flow speed of 2 cm s^{-1} and a high image acquisition speed of 24k lines per s for 4-color SRS signal acquisition. With the help of machine learning to analyse large cell populations (~10 000 cells), the authors demonstrated high-precision characterization and classification of cancer cells in blood at an unprecedented throughput of ~140 cells per s (Fig. 9F).

Four biophysical properties including cell dimension, nucleus-to-cytosol ratio, refractive index of the nucleus and cytosol for each cell were converted from the light-scattering profile and combined with machine learning for automatic counting and characterization of CD4+ *versus* CD8+ with 79% accuracy. In another work, Yoon *et al.* used 3D refractive index (RI) tomography to identify lymphocyte cell types based on quantitative morphological and biochemical properties of individual lymphocytes (Fig. 9G).[160] The novelty of this work is the combination of RI tomography with machine learning to enable the identification of lymphocyte cell types (B, CD4+ T and CD8+ T cells) with high test accuracy (75.93%).

Besides cell imaging, label-free imaging of single exosomes was reported by Yang *et al.* using interferometric plasmonic microscopy (iPM).[161] This was achieved by monitoring the real-time adsorption of exosomes on a modified Au surface and recording the iPM intensity to determine the size distribution by image reconstruction (Fig. 9H). In summary, label-free optical approaches offer numerous advantages in terms of throughput, information-rich cell images, and easier coupling to machine learning for automated blood analysis. The challenges need to be addressed include the precise focusing of cells, efficient removal of bulk RBCs prior to analysis and high setup cost.

Mechanical properties

The cytoskeleton is an interconnected network of protein filaments that provides cell shape, determines cell resistance to deformation, and interacts with the extracellular tissue environment. As it is a dynamic and adaptive structure that is affected by cellular activities, accessing cell mechanics is

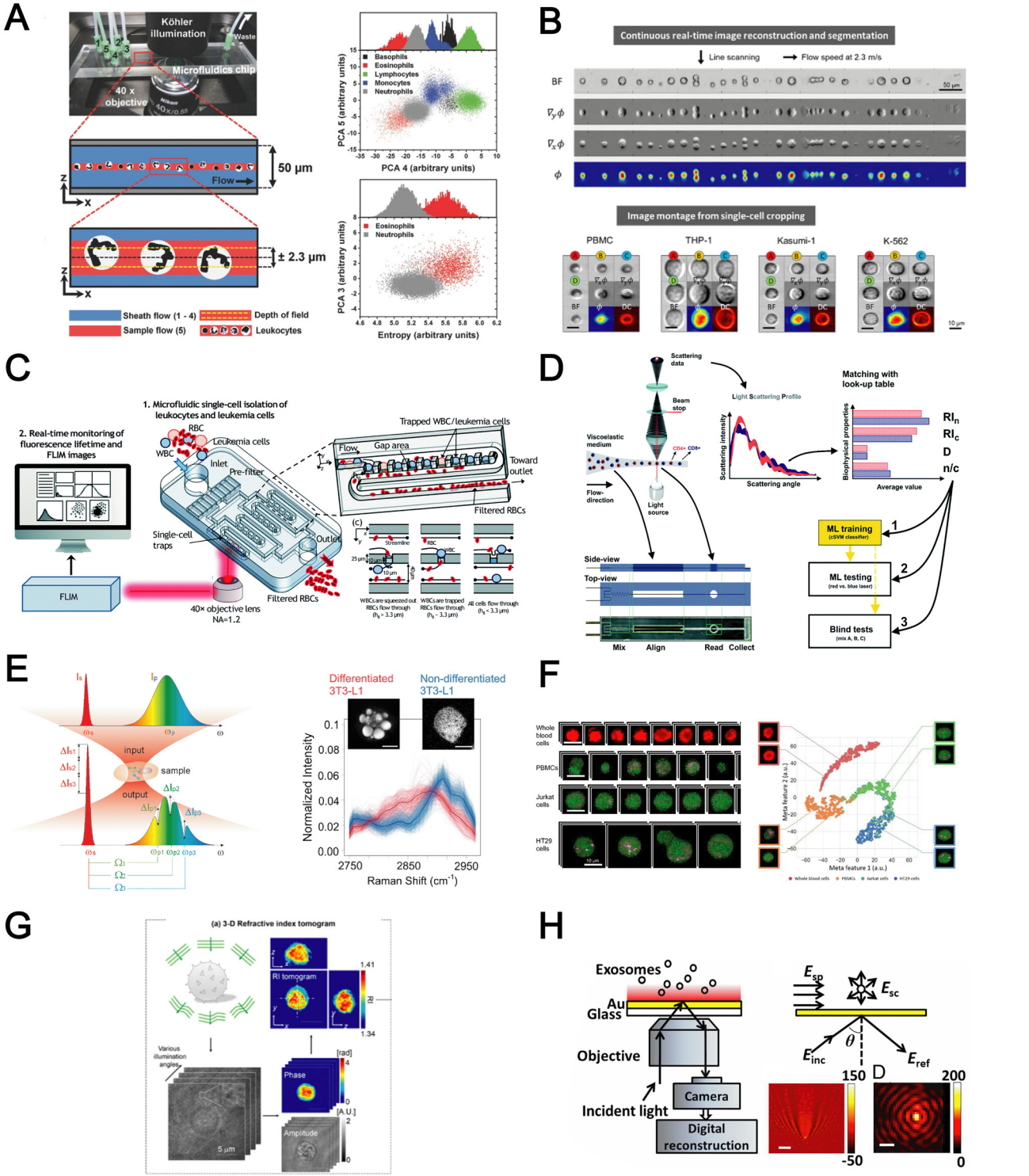

Fig. 9 Label free cell detection based on optical properties. (A) Microfluidic cell presentation and five-part DIFF of leukocytes. Reproduced from ref. 159 with permission from Wiley. (B) Multi-contrast single-cell images captured in the multi-ATOM flow cytometer. Reproduced from ref. 162 with permission from Wiley. (C) Isolation and identification of single leukemia cells from blood based on single-cell trapping and phaser-FLIM imaging. Reproduced from ref. 163 with permission from the Royal Society of Chemistry. (D) Identification of CD4+ and CD8+ T-lymphocytes using light scattering and machine learning. Reproduced from ref. 155 with permission from the Royal Society of Chemistry. (E) Multiplexed stimulated Raman scattering process and SRS spectra of two cell populations. Reproduced from ref. 168 with permission from Optica Publishing Group. (F) SRS images of whole blood cells, PBMCs, Jurkat cells, and HT29 cells. Classification of cancer cells in blood using the t-SNE plot. Reproduced from ref. 169 with permission from the National Academy of Sciences. (G) Identification of individual lymphocytes using optical diffraction tomography. Reproduced from ref. 160 with permission from Nature Research. (H) iPM system for single exosome detection based on interferometric scattering. Images of a 100 nm silica nanoparticle without (left) and with (right) an image-reconstruction process (scale bar: 300 nm). Reproduced from ref. 161 with permission from United States National Academy of Sciences.

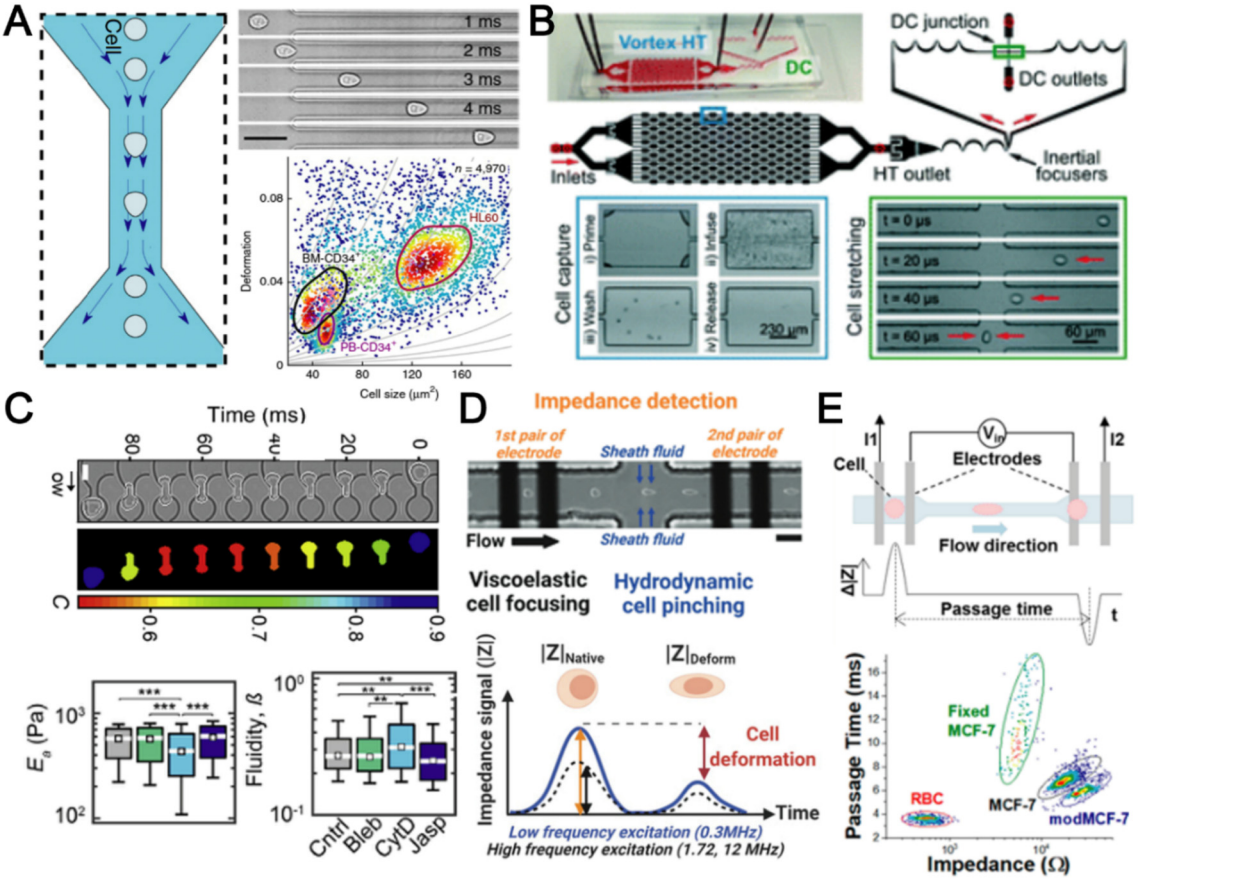

Fig. 10 Label free cell detection based on mechanical properties. (A) Real-time deformability cytometry (RT-DC) that optically quantified cell geometrical change under shear force. Reproduced from ref. 171 with permission from Springer Nature. (B) Vortex-mediated deformability cytometry (VDC) that enriched CTCs and hydrodynamically deformed cells on the same device. Reproduced from ref. 174 with permission from the Royal Society of Chemistry. (C) Quantitative deformability cytometry (q-DC) that utilized creeping energy to quantitatively measure cell intrinsic properties. Reproduced from ref. 177 with permission from Cell Press. (D) Impedance deformability cytometry that represented cell deformation with impedance signatures. Reproduced from ref. 178 with permission from Wiley. (E) Impedance-based deformability cytometry that quantified cell transition time in the constriction channel with impedance signatures. Reproduced from ref. 182 with permission from the American Chemical Society.

important to study mechanobiology and pathophysiology.[170] In this section, we highlight recent advances in microfluidics deformability cytometers for label-free blood cell profiling.

The most direct approach to quantify cell deformability is to image single cell geometrical changes under mechanical stimuli such as shear force,[171] hydrodynamic force,[172] and electric force.[173] Otto *et al.* reported a real-time deformability cytometry (RT-DC) platform that quantifies cell circularity change under shear force using high-speed imaging (Fig. 10A).[171] Cell mechanical phenotypes (cell size, deformability) and their sensitivity to cytoskeleton changes were measured and used as biomarkers to identify PBMCs, RBCs, granulocytes, and platelets from whole blood directly. To analyse rare cell events, Che *et al.* reported a vortex-mediated deformability cytometry (VDC) platform that performed on-chip circulating tumour cell (CTC) enrichment and deformability assessment directly from whole blood (Fig. 10B).[174] Their results showed a better CTC detection rate (93.8%) using the biophysical phenotypes (cell size, deformability) as compared to affinity-based immunofluorescence (71.4%). Besides cell profiling for drug treatment study[175] or point-of-care diagnostics,[8,176] cell mechanical properties such as Young's modulus and fluidity can also be determined if calibrated with known reference materials. For example, Nyberg *et al.* applied quantitative deformability cytometry (q-DC) to optically track cell geometrical changes to study cell creeping (Fig. 10C).[177] After calibration with agarose gel particles, a power-law rheology (PLR) model was used to represent cell creeping in the constriction channel to extract quantitative information on cell elasticity and fluidity of leukaemia cells (HL-60). To avoid the use of expensive high-speed cameras, researchers have developed impedance-based detection methods to profile cell biophysical properties by quantifying the cell geometrical change,[178] or cell creeping process[179] in an optics-free and label-free manner. A recent study was reported by Petchakup *et al.* who defined a novel "electrical deformability index" for single cell electro-mechano-phenotyping (Fig. 10D).[178] By measuring electrical signals at different frequencies (0.3 MHz, 1.72 MHz and 12 MHz), multiple biophysical parameters of single cells such as cell size, deformability,

membrane opacity and nucleus opacity are simultaneously measured to study neutrophil dysfunction.

Besides quantifying changes in cell shape, another approach to analyse cell deformability is by measuring cell transit time in constriction channels using imaging,[180] suspended microchannel resonators (SMRs),[181] and impedance readout.[182] For example, impedance signals are detected when a cell passes through electrodes at the start and end of the channel to calculate cell transition time (Fig. 10E).[182] Clear differences between RBCs and cancer cells (MCF-7 and modified MCF-t (softer)) were observed by comparing the cell impedance magnitude and cell

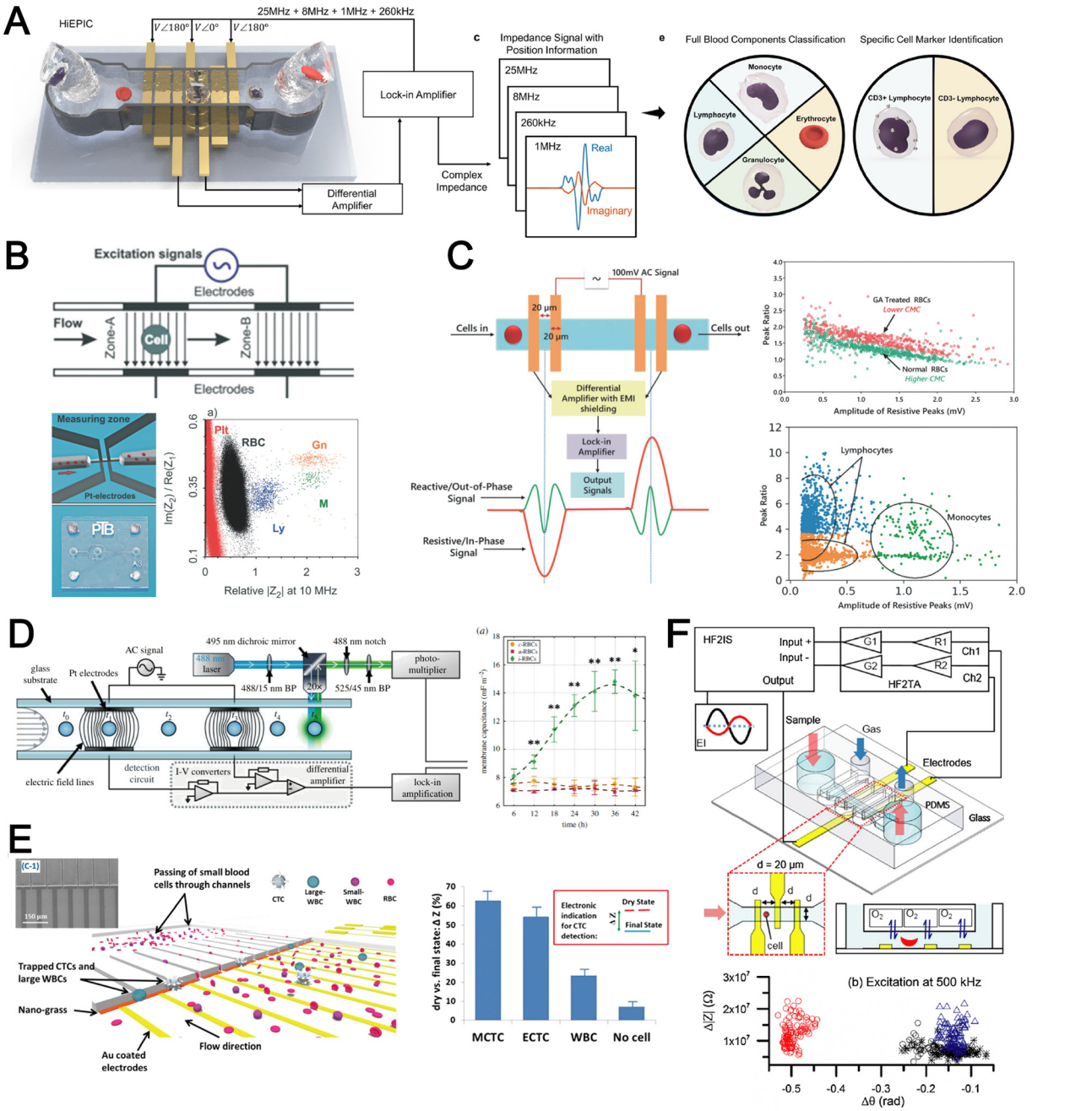

Fig. 11 Label free cell detection based on electrical properties. (A) Top and bottom parallel electrode configuration for label-free discrimination of platelets, erythrocytes, monocytes, granulocytes and lymphocytes. Reproduced from ref. 190 with permission from Elsevier. (B) Copland electrodes for cell classification using single frequency. Reproduced from ref. 193 with permission from the Royal Society of Chemistry. (C) Microfluidic impedance cytometry for dielectric characterization of *Plasmodium falciparum*-infected red blood cells. Reproduced from ref. 194 with permission from the Royal Society of Chemistry. (D) Microfluidic impedance spectroscopy device with trapping design for diagnosis of CTCs. Reproduced from ref. 195 with permission from the Royal Society. (E) Impedance microfluidic cytometer with oxygen control for detection of sickle red blood cells. Reproduced from ref. 197 with permission from Wiley. (F) HiEPIC system for blood cell classification. Reproduced from ref. 199 with permission from Elsevier.

deformability. However, major challenges include clogging issues and the requirement for low working sample concentration to avoid multiple cells entering the constricted channel. For RBC analysis, microfluidics deformability studies are typically performed in batch analysis to determine an average deformability score based on batch deforming pressure,[183] relative lateral displacement,[184] and filtration gap size.[185] In summary, label-free biophysical profiling of WBCs and RBCs is highly promising for low-cost blood phenotyping. Future work will focus on extending the mechanical cellular assessment to small particles such as platelets and EVs.

Electrical properties

The cell membrane and intracellular content exhibit distinct dielectric and electrical properties for different cell types which can be exploited for label-free single cell detection. A powerful electrical biosensing modality is impedance cytometry which takes advantage of the dielectric dispersion effect under alternating electric field at varying frequencies to characterize different cellular components. It is widely applied for single cell analysis including cell classification and counting,[186,187] and cell status monitoring.[188,189]

The impedance magnitude and opacity (ratio of impedance magnitudes at different frequencies) are the most frequently used signatures for cell characterization. Conventional microfluidic impedance cytometers utilize 2D coplanar electrodes for impedance measurement,[186,187] but the signal is affected by the vertical position of the particles in the channel. Zhong *et al.* proposed a high throughput (1000 cells per second) and position-insensitive coplanar electrode-based cytometry platform with a double differential electrode configuration (Fig. 11A). The additional position information provided by this novel electrode configuration contributes to a higher accuracy of cell detection to classify different leukocyte subtypes.[190,191] A complicated electrode configuration with two pairs of parallel (top and bottom) electrodes and three additional pairs of co-planar electrodes is also proposed to minimise the effect of particle position on the signal magnitude by reducing the cross current flow into neighbouring detection electrodes.[192] This work demonstrated successful classification and numeration of different leukocytes from human blood after erythrocyte lysis. Another strategy is using a 3D parallel electrode configuration to differentiate platelets, erythrocytes, monocytes, granulocytes and lymphocytes in blood by two pairs of top and bottom parallel electrodes (Fig. 11B).[193] In addition to impedance-based cell detection, simultaneous capture of cell size and membrane property at single low frequency was reported by Mahesh *et al.* (Fig. 11C).[194] They showed the relationship between the cell membrane capacitance and the 'double peak' profile in the out-of-phase signal within low frequencies (beta dispersion regime) to distinguish normal RBCs and glutaraldehyde-treated RBCs based on a single frequency signal measurement.

Besides blood profiling, impedance cytometry is also used for blood-based disease detection. For example, malaria-infected RBCs (*Plasmodium falciparum*) have higher membrane capacitance and cytoplasmic conductivity which would be useful for pre-enrichment of infected RBCs for malaria diagnosis (Fig. 11D).[195] Application of impedance cytometry for CTC detection in whole blood has also been reported with integrated CTC trapping (Fig. 11E)[196,197] or under continuous flow.[198] Liu *et al.* developed a microfluidic chip allowing oxygen control for the detection of sickle red blood cells (Fig. 11F).[199] Interestingly, significant differences in impedance profile were revealed between normal cells and sickle cells under normoxia, and between sickle cells under normoxia and hypoxia.

In summary, impedance-based detection is a promising label-free blood cell analysis technique which does not require expensive high-speed camera imaging. Although the signal is generally dependent on particle position in microchannels, recent advances have achieved higher sensing sensitivity through better electrode configurations and channel structures, as well as developing new signal processing strategies. Future work will focus on improving electrode fabrication and the calibration using reference materials for large-scale clinical testing.

Label-free cell analysis using machine learning approaches

Machine learning (ML) is a field of computer algorithms that can learn relations of data without explicit programming or human intervention. With enhanced computing power and data storage, ML has gained increasing attention for a wide variety of biomedical applications especially in biomarker discovery[200] and clinical diagnostics.[201] Emerging applications of ML to synergize microfluidics include optimizing device design, operation and data processing/analysis. ML can be used to construct microfluidic design models based on experimental performance metrics (*e.g.* sorting efficiency, yield) and channel features (*e.g.*, channel geometry, flow rate) to improve design performance or predict the behavior of new samples. This can potentially ease the iterative device optimization process and lower manufacturing and testing costs.[127] Microfluidic devices integrated with imaging/sensing modalities (*e.g.*, camera, electrodes, flow/pressure sensors) can incorporate ML to analyze real-time information (*e.g.*, particle trajectory, particle properties, flow rate, pressure drop) "on-the-fly" and provide feedback to pumps/actuators for automated flow manipulation or resolving operational issues (*e.g.* channel clogging). These aspects have been extensively covered in a recent review by McIntyre *et al.*[202] Lastly, ML can enhance the data analysis pipeline in preprocessing steps such as feature extraction or denoising, as well as in postprocessing steps including developing a prediction model and compressing multi-dimensional data for visualization.

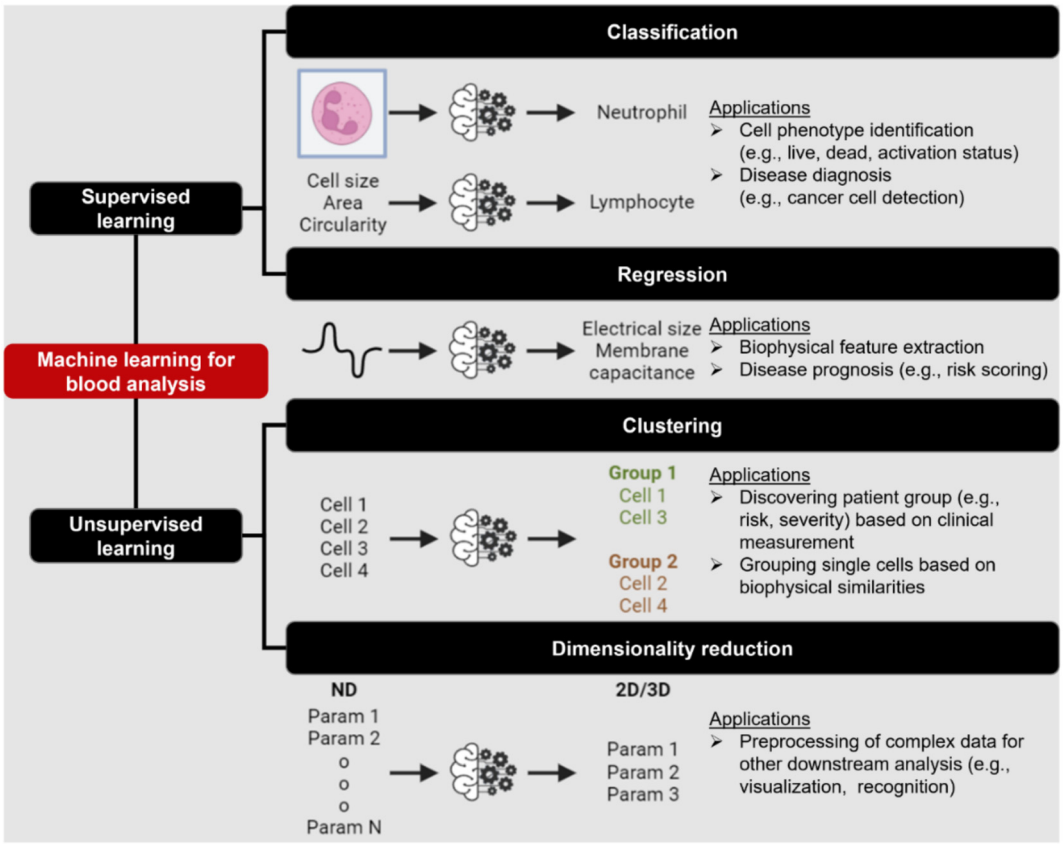

Fig. 12 Overview of machine learning (ML) utilities in microfluidic label-free sensing.

As label-free cell characterization may lack specificity and sensitivity compared to antibody-based detection, multi-parametric analysis of intrinsic cell properties combined with advanced data analysis can potentially improve the assay accuracy. In this section, we will highlight recent work that utilize ML for microfluidics label-free blood cell phenotyping in two broad classifications, namely 1) supervised learning and 2) unsupervised learning (Fig. 12 and Table 5). For more detailed information, the readers are highly encouraged to refer to other excellent reviews for microfluidic applications[203–205] and neural networks/deep learning.[206,207]

Supervised learning

Supervised learning aims to establish connections between example inputs (*e.g.*, image, signal, and data) and their corresponding outputs such as labels (cell types, pathological phenotypes) or single cell features (single cell properties, shape) for classification or regression problems, respectively. Traditionally, classification pipelines include preprocessing (filtering) and feature extraction to extract single cell features (*e.g.*, single cell properties) followed by training a classifier to recognize labels from extracted features.[206] The choice of classifier can vary based on applications and data complexity. Popular classifiers mentioned in the literature are tree-based model (*e.g.*, decision tree, random forest), support vector machine (SVM) and neural networks. With the emergence of deep learning,[207] the classification problem is greatly simplified as deep neural networks are capable of learning crucial representative features for classification directly from raw inputs without the need for preprocessing or feature extraction. To improve the performance of the model built with small-size data, one can also make use of transfer learning in which a pretrained model from one task can be used as a building block for another model for a similar task.[208] Here we list the utilities of supervised learning based on input types (image, signal and data) as shown in Fig. 13.

Image input. Convolutional neural network (CNN) is a powerful technique for any computer vision tasks because of its ability to learn elementary features (*e.g.*, edges, corner *etc.*) and more complicated features such as parts of objects/objects in different shapes and locations in the image. This can be readily applied to any imaging modalities (brightfield, autofluorescence). For example, Nitta *et al.* developed an intelligent high-speed imaging flow cytometer for classification of leukocytes, platelets, and platelet aggregates showing a high specificity and sensitivity of 99.0% and 82.0% (Fig. 13A).[166] Kräter *et al.* also performed classification of blood components (97.3% validation accuracy) and T-cells/B-cells (86.2% testing accuracy) using biophysical images using a deformability cytometry.[209] Kobayashi *et al.* demonstrated an interesting application for drug susceptibility testing by

Table 5 List of machine learning applications for blood analysis using microfluidics

Category	Technique	Samples	Features	Applications	Ref.
Classification or regression	SVM with RFE	WBC, MCF-7, HL-60	Features extracted from brightfield images from deformability cytometer	Classification of spiked cancers with WBC with <5% error in classification rate for differently mixed samples	246
	Logistic regression	WBC, PLT and PLT aggregate	Morphological features from brightfield image	Classification with specificity of 96.6%	247
	Decision tree	PBMCs, MCF-7 and MDA-MB231	Cell size, maximum intensity, and mean intensity	Cell classification with AUROC >0.9 for all features	217
	Decision tree, SVM, LDC and *k*-NN	RBC (discocyte, echinocyte and spherocyte)	Features from DIHM (12D)	Comparison of classification algorithms and decision tree achieved the best accuracy (98.18%)	248
	CNN	WBC, PLT and PLT aggregate	Brightfield image	Classification of PLT aggregate with specificity of 99% and selectivity 82%	166
	N/A	PBMC/THP-1, Kasumi-1 and K-562	Features extracted from QPI (12D)	Classification with 94% accuracy. AUROC for one-*versus*-all classification were 0.975/0.920, 0.95 and 0.952 for PBMC, THP-1, K-562 and Kasumi-1, respectively	249
	CNN (autoencoder)	K562, K562/ADM cells and RBC	Brightfield image	Quantification of drug-induced morphological changes and segmentation of RBC and cancer cells from the images with 86% pixel-wise accuracy	210
	CNN	Whole blood cells, PBMCs, Jurkat cells, and HT29 cells	Stimulated Raman scattering images	Classification accuracy of >93%	250
	RNN (LSTM-NN)	RBCs and beads	Impedance signal measured in horizontal and vertical direction	Extraction of diameter velocity and positions of cells	213
	NN	PBMC, small cell lung cancer (NSCLC)	80 optofluidic features from brightfield and quantitative phase imaging	Detection of spiked NSCLC (H2170) PBMC with 98% accuracy	219
	SVM	WBC, SW480 and SW620	Optical phased delay features	Classification sensitivity, specificity, and accuracy of 97.8%, 98.9% and 99.6%, respectively	251
	SVM	CD4 and CD8 T-lymphocytes	Features from light scattering profile (size, nucleus-to-cytosol ratio, refractive index of nucleus and cytosol)	Classification with 70.31% and 87.10% for unstimulated and stimulated cells, respectively	252
	NN	Neutrophils, RBCs	Images from RT-FDC	Classification of neutrophils with 95.5% accuracy	253
	CNN	WBC subtypes	Brightfield images from RT-DC	Classification of blood cells and classification of T-cells and B-cells (transfer learning from Nitta *et al.*[166])	209
	SVM	RBC	Features extracted from trained CNN (AlexNET)	Classification of different kinds of anemia (SCD, THAL and HS)	227
	SVM with radial basis function	WBC from healthy and sepsis patients	38 biophysical markers quantified from DLD-devices at different flow rates and designs	Prediction of sepsis infection with AUROC of 0.97	218
	CNN	RBC	Brightfield images	Classification of deformable and non-deformable sickle RBC and non-sickle RBC with accuracy of 96% ± 0.3%	254
	CNN	RBC	Images	Classification of RBC from different outlets and determine RBC rigidity score	255
	CNN	Bead, RBC and ghost RBC	Impedance images (stacked impedance signal at 8 frequencies)	Classification, calibration of measurement using bead properties and extraction of electrical parameters (cell size, membrane capacitance and cytoplasm permittivity and conductivity)	212
	NN	WBC	Impedance parameters (cell size, membrane capacitance, cytoplasmic conductivity)	Classification with 93.5% accuracy	216
	NN	WBC including eosinophils and basophils	Impedance parameters (cell size, membrane capacitance, cytoplasmic conductivity)	Classification rate of 80.8% for neutrophil *vs.* eosinophil, 77.7% for neutrophil *vs.* basophil and 59.3% for neutrophil *vs.* basophil	215
	NN	MCF-7, A549, HeLa, HL60 and GM12878	Impedance peaks at four different frequencies	Extraction of electrical properties and classification with 91.5% accuracy	256
	CNN	WBC	Brightfield images	Classification with 81.4% accuracy	257

Table 5 *(continued)*

Category	Technique	Samples	Features	Applications	Ref.
	MASK-RCNN, CNN–GRU	HL-60 (untreated, cytochalasin D and nocodazole)	Brightfield images	Segmentation using Mask-RCNN and classification of image sequence using CNN–-GRU with accuracy of over 90%	211
Clustering	DBSCAN	WBC and bead	Impedance parameters (cell size and opacity)	Extraction of cell cluster from heterogenous population	189
	GMM	HL-60 cells and MG-63	Area and deformability from RT-DC	Cluster cell populations in mixtures	224
	Hierarchical clustering	WBC from healthy and sepsis patients	38 biophysical markers quantified from DLD-devices at different flow rates and designs	Group patients into 8 groups	218
Dimensionality reduction	t-SNE	PBMC/THP-1, Kasumi-1 and K-562	Features extracted from QPI (12D)	Visualization of cell type distribution in 2D t-SNE	249
	PCA	PBMC, small cell lung cancer (NSCLC)	80 optofluidic features from brightfield and quantitative phase imaging	Visualization of spiked H2170 distribution in 3 dimensions-PCA	219
	PCA	WBC, SW480 and SW620	Optical phased delay features	Visualization cell distribution in 3 dimensions-PCA	251
	PCA	WBC from healthy and sepsis patients	38 biophysical markers quantified from DLD-devices at different flow rates and designs	Visualization of healthy and sepsis patient data	218
	Pre-trained CNN (AlexNET)	RBC	Brightfield image	Extraction of latent features from brightfield image	227
	UMAP	Neutrophils (untreated, apoptosis, necrosis and NETosis)	Impedance-deformability parameters (10D)	Visualization of different neutrophil phenotypes in 2D UMAP	178

first constructing a convolutional autoencoder for segmentation of leukemia cells (K562 or K562/ADM cells) and RBCs in whole blood directly from brightfield images in which they achieved 86% of pixel-wise accuracy (Fig. 13B).[210] They then made use of the latent space from the bottle-neck layer of the trained autoencoder to assess drug-induced morphological changes of the cells using maximum mean discrepancy (MMD) and the Hilbert–Schmidt independence criterion (HSIC), and found that these parameters reflect the effect of drug concentration on cell morphology. Employing temporal models to perform classification based on dynamic cell phenotypes from images or videos is another interesting utilization.[211] They developed a microfluidic device with an undulating channel (expansion and contraction regions) to optically observe cell deformation in viscoelastic medium. To facilitate their image analysis, they introduced Mask-RCNN to segment cells in brightfield images and constructed CNN with a gated recurrent unit (GRU) to perform classification of different HL-60 phenotypes (untreated, CytoD-treated and nocodazole-treated) from the sequence of segmented images. The model achieved over 90% accuracy and performed better than random forest and SVM using shape descriptors of cells at different stages.

Signal input. The time-series signal from impedance or optical cytometric sensors conveys single cell information that can lead to cell type classification. Caselli *et al.* proposed a comprehensive NN pipeline to handle multi-frequency impedance signals (magnitudes and phases) for 1. measurement calibration, 2. discrimination between beads and RBCs, and 3. extraction (regression) of single cell electrical parameters such as cell size, cytoplasm conductivity, membrane capacitance (Fig. 13C).[212] Other notable utilities are classification of multiple particles in detection zones (*e.g.*, singlet, doublet),[212] extraction of velocity and position[213] and extraction of electrical measurement from multiple channels.[214]

Feature input. Extracted features from single-cell images or signals can be used for classification of leukocytes.[215,216] For example, Singh *et al.* employed features extracted from holographics for classification of the PBMC and tumor cell line using decision tree.[217] Another interesting work is from Zeming *et al.* in which the authors employed DLD extracted biophysical features of patient blood for classification of sepsis infection using support vector machine (SVM) classification using radial basis function kernel (AUROC 0.97).[218] Siu *et al.* utilized 80 optofluidic features from QPI and brightfield images which measure bulk and subcellular texture information for identification of spiked NSCLC (H2170) in PBMCs using deep neural network with 98% accuracy which was better than using size alone or other bulk features (Fig. 13D).[219] Tan *et al.* used neural network to classify leukocytes based on single electrical features (diameter, specific membrane capacitance and cytoplasmic conductivity) derived from a constriction-based impedance cytometer.[216]

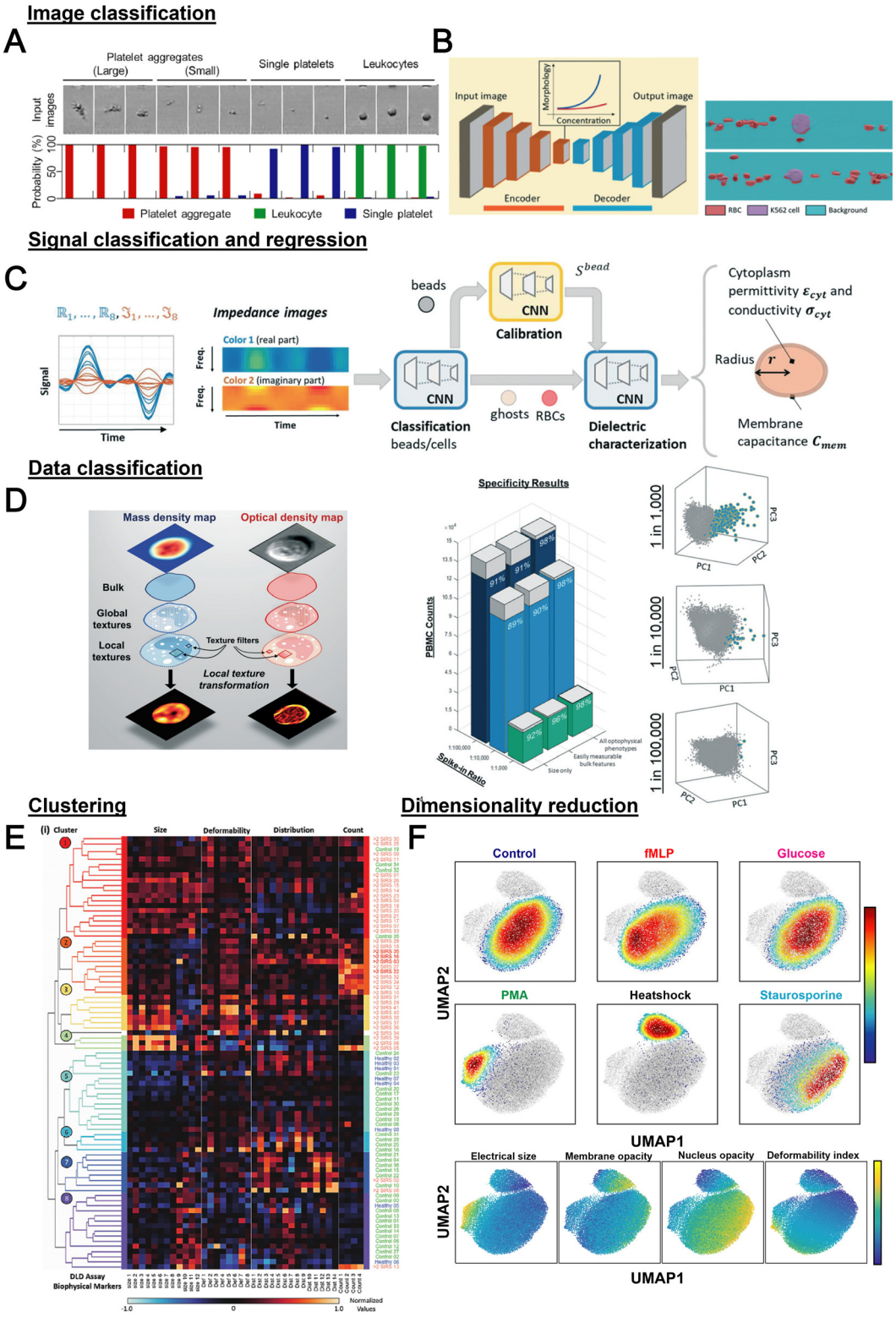

Fig. 13 Machine learning for blood analysis. (A) Image classification of leukocytes and platelet aggregates from brightfield images captured from an intelligent flow cytometer. Reproduced from ref. 166 with permission from Elsevier. (B) Convolutional autoencoders for cancer cell and RBC segmentation and assessment of drug-induced morphological changes using maximum mean discrepancy (MMD). Reproduced from ref. 210 with permission from the Royal Society of Chemistry. (C) Integrated framework for multifrequency impedance signal processing for classification of beads, RBCs and ghost RBCs and extraction of electrical properties of single cells. Reproduced from ref. 212 with permission from the Royal Society of Chemistry. (D) Classification of spiked NSCLS in PBMC samples using opto-physical features from QPI and brightfield images. Reproduced from ref. 219 with permission from the Royal Society of Chemistry. (E) Hierarchical clustering for grouping of DLD extracted measurement for sepsis analysis. Reproduced from ref. 218 with permission from Wiley. (F) Dimensionality reduction using UMAP to compress electrical-based biophysical parameters for visualization of different neutrophil phenotypes. Reproduced from ref. 178 with permission from Wiley.

Many ML models are viewed as a black box model as it can be difficult to comprehend how models reach their final outcomes which may fail to attract trust and acceptance for clinical uses.[220] To improve interpretability and explainability of a model, certain approaches can be done including feature importance (*e.g.*, Shapley value,[221] permutation importance[222]) to understand the contribution/weight of features on a final prediction, or attention mechanism (*e.g.*, class activation map (CAM)[223]) to visualize which part of an image that influences a class prediction.

Unsupervised learning

In contrast to supervised learning, unsupervised learning can learn patterns/structures from unlabeled data and be categorized as either clustering or dimensionality reduction (Fig. 14). Clustering involves grouping of unlabeled data/features into several groups based on certain similarity metrics (*e.g.*, Euclidean distance, cosine similarity) or distributions. For example, density-based spatial clustering of applications with noise (DBSCAN) can be used to group single cell electrical features and extract a target cell population for quantification.[189] Herbig *et al.* employed Gaussian mixture models (GMM) to cluster HL-60 cells and MG-63 from cell mixtures based on the area and deformability extracted from cell deformability measurements.[224] Hierarchical clustering was also applied to group patients based on the similarities of their DLD biophysical parameters and certain cluster groups were shown to correlate with long hospitalization stay (Fig. 13E).[218]

Dimensionality reduction simplifies high dimensional data into low-dimensional data (usually 2, 3 dimensions) for data visualization and analysis. In some scenario,

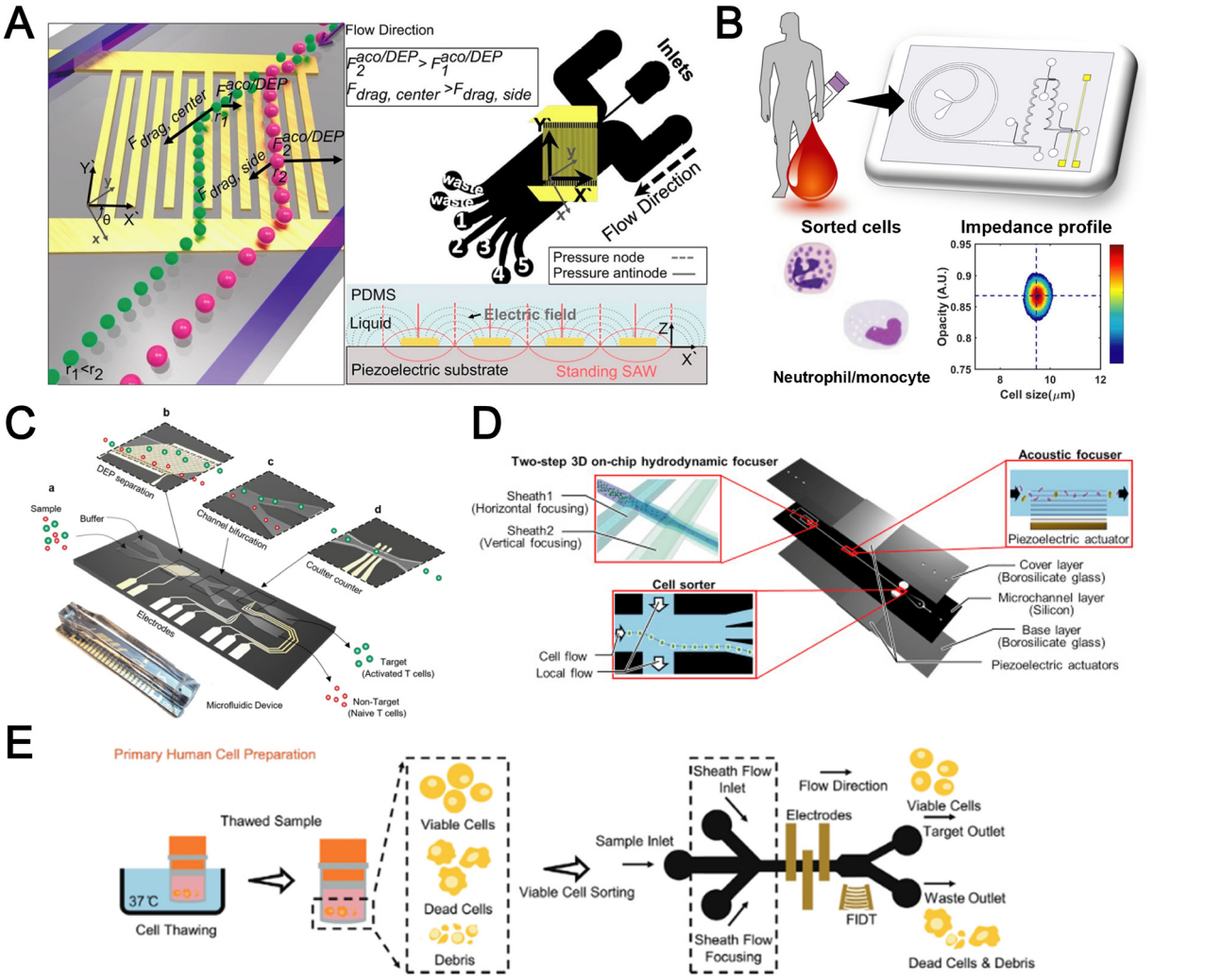

Fig. 14 Integrated microfluidic platforms for blood applications. (A) Integrated acoustic and DEP for exosome separation. Reproduced from ref. 130 with permission from the American Chemical Society. (B) Integrated inertial impedance cytometer. Reproduced from ref. 189 with permission from the Royal Society of Chemistry. (C) DEP-impedance cytometer for differential counting of activated lymphocytes. Reproduced from ref. 233 with permission from the American Chemical Society. (D) Intelligent imaging flow cytometer. Reproduced from ref. 166 with permission from Elsevier. (E) Impedance activated surface acoustic wave cell sorter. Reproduced from ref. 235 with permission from Wiley.

having numerous features does not always guarantee an increase in predictive performance and can even deteriorate performance of certain models. This is because adding more features makes feature space more sparse and difficult for models to generalize (curse of dimensionality). Introducing dimensionality reduction as an intermediate step prior to other ML techniques can alleviate dimensionality issues. Techniques such as principal component analysis (PCA), t-distributed stochastic neighbor embedding (t-SNE) and uniform manifold approximation and projection (UMAP) are widely used in flow cytometry analysis and biological studies.[225,226] Inspired by these methods, Petchakup *et al.* utilized UMAP to visualize biophysical features of different neutrophil phenotypes (Fig. 13F).[178] Another way to harness the power of transfer learning is to exploit pre-trained CNN for feature extractor. As pre-trained CNNs (*e.g.*, AlexNET) are trained from a large-scale image dataset, it has already captured all important features or patterns. By passing image input (high-dimensional data) through a pre-trained network, it can output the latent features (low-dimensional data) which can be used in the subsequent task.[227] They used trained CNN to extract features from brightfield images of RBCs and subsequently SVM for classification of different RBC phenotypes such as sickle cell disease (SCD), thalassemia syndromes (THAL) and hereditary spherocytosis (HS).[227]

Taken together, these exciting studies have shown that ML can enhance blood analysis. It is possible to develop an intelligent microfluidic system to provide fast, automated, and accurate analysis without the need for clinical expertise or mechanistic biological knowledge. It should be noted that to produce a model with good generalization, large data collection is sometimes required, and comes with the cost of additional time and resources (biological samples, donor samples). Implementing ML for analysis usually incurs additional computational resources (processors) which may compromise the overall system setup (footprint). As ML exponentially evolves, other novel ML utilities have also been reported for biomedical image analysis including "virtual staining"[228] in which CNNs were designed to understand the associations between morphological features of label-free images (*e.g.*, autofluorescence, brightfield) and stained images (histological, antibody stained) for image-to-image translation to produce stained images without the need for laborious staining. A potential use for blood cell analysis is to construct a virtual staining model of subcellular components such as the nucleus and mitochondria in single immune cells for label-free quantification applications. It is also possible to use generative models to synthesize more training data (*e.g.*, biomedical images) to improve predictive model generalization.[229] This can be readily adopted to produce more events of rare cells especially CTCs from microfluidic assays to improve a predictive model.

Integrated label-free blood cell sorting and analysis

A powerful aspect of microfluidics is to miniaturize and integrate sample preparation and biological assays on a single chip to automate medical analysis. Herein, we highlight several integrated microfluidic approaches for complete label-free blood analysis (Fig. 14).

Multiparametric sorting or sensing

To achieve higher separation efficiency, one can combine multiple sorting mechanisms to enhance particle separation. For example, Tayebi *et al.* combined acoustic and DEP forces for exosome separation (Fig. 14A).[130] The ability to interrogate various single cell features is crucial for single cell analysis for elucidating immune cellular functions or disease pathology using multi-colour flow cytometry.[230] As intrinsic or biophysical features obtained from single measurement might be limited, multi-parametric single cell measurement is important to enhance assay sensitivity or for ML applications. A common pairing is mechanical measurement with optical or impedance detection as changes in cell mechanics are often reflected in cell morphology which can be quantified using image or impedance readout. For example, Petchakup *et al.* demonstrated single cell electro-mechano-phenotyping (14 biophysical parameters of single cells) to study different neutrophil phenotypes during activation and apoptosis.[178]

Integrated sample processing

As conventional RBC lysis or density centrifugation steps can be time-consuming and laborious, integrating a sample preprocessing module will facilitate direct blood processing and detection of target cells. An integrated spiral microfluidic chip with an impedance cytometer was used for removal of small blood components (*e.g.*, lymphocytes, platelets and RBCs) to allow electrical interrogation of monocytes, neutrophils or activated lymphocytes from diluted blood or PBMCs (Fig. 14B).[189,231] Raillon *et al.* utilized inertial vortex induced CTC trapping prior to impedance cytometry.[232] Han *et al.* applied DEP for pre-sorting of large, activated-lymphocytes from small native-lymphocytes for subsequent differential impedance counting (Fig. 14C).[233] Another interesting integration is to increase detection specificity by differential counting of target cells before and after traversing a cell capturing chamber functionalized with capture antibodies.[234]

Integrated active sorting

To elucidate associations between label-free features and biological functions, an actuated cell sorter can be added to select cells based on label-free features (impedance, optical, mechanical). A great example is reported by Nitta *et al.* in which they incorporated various microfluidic modalities such as an acoustic focuser and dual membrane push–pull cell

sorter to complement high-speed imaging for platelet aggregate sorting based on morphological features (Fig. 14D).[166] Zhong *et al.* demonstrated acoustic sorting using impedance signatures for live cell sorting from thawed PBMC samples (Fig. 14E).[235]

Conclusions and outlook

In summary, microfluidics or lab-on-a-chip technologies provide numerous advantages including reduced preparation time, small sample and reagent volume requirements, precise control over the cell microenvironment and ease of integration. As blood is routinely sampled and contains a rich source of cellular and molecular biomarkers, this review highlights the recent advancements in label-free microfluidic blood cell sorting and analysis for clinical diagnostics. By eliminating the need for expensive antibodies or chemicals, label-free microfluidic assays not only provide valuable insights for intrinsic single cell multi-parameter analysis, but are also essential for identifying cell types and understanding their biological functions. It is especially powerful for blood-based diagnostics as it requires minimal sample preparation and is more cost effective and scalable for clinical testing. Label-free cell sorting often exploits biophysical differences in different cell types to achieve separation and there is a variety of passive or active microfluidic methods reported for blood fractionation. Label-free cell detection approaches include optical measurement of cell morphology and intracellular components, impedance cytometry to detect cellular and sub-cellular electrical properties at multiple frequencies, as well as quantifying cellular mechanics (*e.g.* cell deformability) which can be indicative of cell dysfunction in diseases. While label-free cell detection may lack specificity and sensitivity as compared to affinity-based (*e.g.* antibodies) methods, recent studies have greatly improved their detection accuracy and clinical utilities by enabling multi-parametric cell analysis and high dimensional data processing. Coupled with machine learning approaches, they are highly promising for automated high-throughput blood analysis and biomarker discovery in biomedical research.

Numerous technological advancements have been demonstrated for both label-free blood cell sorting and detection. Besides improving sample throughput and separation performance, integrated and user-friendly microfluidic systems will be key to automate and scale up for high throughput clinical samples testing. Especially for label-free separation approaches, multi-physics or multi-stage cell sorting can potentially refine resolution separation with the trade-off of increased device complexity. For example, isolation of immune cells from whole blood can be initial RBC bulk removal by cell size differences using inertial focusing or ferrofluids, followed by 2nd step fractionation of leukocyte subtypes (*e.g.*, neutrophils and monocytes) based on other biophysical properties (*e.g.* cell density) by acoustophoresis. To achieve a complete label-free "sample-in-answer-out" microfluidic platform, multiple functionalities (sorting, sensing and analytics) can be integrated to enable high-content and high throughput analysis of multiple blood components. Nevertheless, microfluidic integration is a non-trivial task. Besides having increased complexity in chip design and instrumentation, researchers have to consider flow rate disparity between sorting and detection modules governed by different working principles. Several studies have shown that it is useful to include an additional flow focuser to align cells and siphon excess particle-free medium to reduce the flow rate. Secondly, incorporation of active sorting elements (DEP, acoustic) requires additional equipment and it is important to consider their miniaturisation for point-of-care testing. Lastly, certain techniques such as DEP and viscoelastic flow use specific medium conditions (*e.g.*, conductivity, viscosity) by adding chemicals to blood samples. Combining upstream buffer exchange or particle sorting can help alleviate this issue. We envision that ML-powered microfluidics will improve device operation and robustness and significantly leverage label-free biophysical/chemical features of circulating cellular targets as novel blood-based biomarkers.

Taken together, label-free microfluidics technologies enable new assay development to identify novel biomarkers and non-traditional risk factors in disease diagnostics. By offering a complete label-free blood sample preparation and analysis workflow (cell sorting, cell detection, machine learning methods), we are optimistic that this will reduce barriers to adoption and better guide the readers to develop new clinical applications in liquid biopsy.

Author contributions

Nan Lu: conceptualization, literature search, writing – original draft, review and editing. Hui Min Tay: conceptualization, literature search, writing – original draft, review and editing. Chayakorn Petchakup: literature search, writing – original draft. Linwei He: literature search, writing – original draft. Lingyan Gong: literature search, writing – original draft. Kay Khine Maw: literature search, writing – original draft. Sheng Yuan Leong: literature search, writing – original draft. Wan Wei Lok: literature search, writing – original draft. Hong Boon Ong: literature search, writing – original draft. Ruya Guo: literature search, writing – original draft. King Ho Holden Li: funding acquisition, writing – review & editing. Han Wei Hou: conceptualization, funding acquisition, project administration, supervision, writing – review & editing.

Conflicts of interest

The authors have declared that no conflict of interest exists.

Acknowledgements

The authors would like to acknowledge support from Singapore Ministry of Education Academic Research Fund (MOE AcRF) Tier 2 (MOE-T2EP30120-0004) and under the

RIE2020 Industry Alignment Fund – Industry Collaboration Projects (IAF-ICP) Funding Initiative, as well as cash and in-kind contributions from the industry partner, HP Inc., through the HP-NTU Digital Manufacturing Corporate Lab. Schematics were created with **https://BioRender.com**.

References

1 Z. T. Yu, K. M. Aw Yong and J. Fu, *Small*, 2014, **10**, 1687–1703.
2 H. N. Iskandar and M. A. Ciorba, *Transl. Res.*, 2012, **159**, 313–325.
3 J. M. Rhea and R. J. Molinaro, *MLO Med. Lab. Obs.*, 2011, **43**, 10–12, 16, 18; quiz 20, 22.
4 S. A. Jamali, M. T. Turnbull, T. Kanekiyo, P. Vishnu, A. C. Zubair, C. C. Raper, R. G. Tawk and W. D. Freeman, *J. Stroke Cerebrovasc. Dis.*, 2020, **29**, 104631.
5 H. M. Tay, R. Dalan, K. H. H. Li, B. O. Boehm and H. W. Hou, *Small*, 2018, **14**, 1702832.
6 H. W. Hou, C. Petchakup, H. M. Tay, Z. Y. Tam, R. Dalan, D. E. K. Chew, K. H. H. Li and B. O. Boehm, *Sci. Rep.*, 2016, **6**, 29410.
7 M. Kubánková, B. Hohberger, J. Hoffmanns, J. Fürst, M. Herrmann, J. Guck and M. Kräter, *Biophys. J.*, 2021, **120**, 2838–2847.
8 L. Guillou, R. Sheybani, A. E. Jensen, D. Di Carlo, T. S. Caffery, C. B. Thomas, A. M. Shah, H. T. K. Tse and H. R. O'Neal, Jr., *PLoS One*, 2021, **16**, e0246980.
9 H. M. Tay, W. H. Yeap, R. Dalan, S. C. Wong and H. W. Hou, *Anal. Chem.*, 2018, **90**, 14535–14542.
10 L. Tan, Q. Wang, D. Zhang, J. Ding, Q. Huang, Y.-Q. Tang, Q. Wang and H. Miao, *Signal Transduction Targeted Ther.*, 2020, **5**, 33.
11 Y. Mei, S. E. Weinberg, L. Zhao, A. Frink, C. Qi, A. Behdad and P. Ji, *EClinicalMedicine*, 2020, **26**, 100475.
12 D. Zhang, R. Guo, L. Lei, H. Liu, Y. Wang, Y. Wang, H. Qian, T. Dai, T. Zhang, Y. Lai, J. Wang, Z. Liu, T. Chen, A. He, M. O'Dwyer and J. Hu, *J. Leukocyte Biol.*, 2021, **109**, 13–22.
13 B. B. Nkambule, V. Mxinwa, Z. Mkandla, T. Mutize, K. Mokgalaboni, T. M. Nyambuya and P. V. Dludla, *BMC Med.*, 2020, **18**, 357.
14 E. C. Mesquita, E. D. Hottz, R. T. Amancio, A. B. Carneiro, L. Palhinha, L. E. Coelho, B. Grinsztejn, G. A. Zimmerman, M. T. Rondina, A. S. Weyrich, P. T. Bozza and F. A. Bozza, *Sci. Rep.*, 2018, **8**, 14999.
15 F. Scudiero, R. Valenti, R. Marcucci, G. D. Sanna, A. M. Gori, A. Migliorini, R. Vitale, B. Giusti, E. D. Vito, G. Corda, R. Paniccia, D. Zirolia, M. E. Canonico and G. Parodi, *J. Am. Heart Assoc.*, 2020, **9**, e016441.
16 C.-H. Chao, W.-C. Wu, Y.-C. Lai, P.-J. Tsai, G.-C. Perng, Y.-S. Lin and T.-M. Yeh, *PLoS Pathog.*, 2019, **15**, e1007625.
17 A. Ojha, D. Nandi, H. Batra, R. Singhal, G. K. Annarapu, S. Bhattacharyya, T. Seth, L. Dar, G. R. Medigeshi, S. Vrati, N. K. Vikram and P. Guchhait, *Sci. Rep.*, 2017, **7**, 41697.
18 M. L. Jones, J. Siddiqui, K. J. Pienta and R. H. Getzenberg, *Prostate*, 2013, **73**, 176–181.
19 M. C. Miller, G. V. Doyle and L. W. Terstappen, *J. Oncol.*, 2010, **2010**, 617421.
20 X. Zhang, X. Yuan, H. Shi, L. Wu, H. Qian and W. Xu, *J. Hematol. Oncol.*, 2015, **8**, 83.
21 C. Castaño, A. Novials and M. Párrizas, *Diabetes/Metab. Res. Rev.*, 2019, **35**, e3107.
22 C. Lässer, S. E. O'Neil, G. V. Shelke, C. Sihlbom, S. F. Hansson, Y. S. Gho, B. Lundbäck and J. Lötvall, *J. Transl. Med.*, 2016, **14**, 181.
23 M. J. Martinez-Bravo, C. J. Wahlund, K. R. Qazi, R. Moulder, A. Lukic, O. Rådmark, R. Lahesmaa, J. Grunewald, A. Eklund and S. Gabrielsson, *J. Allergy Clin. Immunol.*, 2017, **139**, 1186–1194.
24 Z. Lanyu and H. Feilong, *Biomed. Pharmacother.*, 2019, **113**, 108748.
25 D. W. Freeman, N. Noren Hooten, E. Eitan, J. Green, N. A. Mode, M. Bodogai, Y. Zhang, E. Lehrmann, A. B. Zonderman, A. Biragyn, J. Egan, K. G. Becker, M. P. Mattson, N. Ejiogu and M. K. Evans, *Diabetes*, 2018, **67**, 2377–2388.
26 S. A. Melo, L. B. Luecke, C. Kahlert, A. F. Fernandez, S. T. Gammon, J. Kaye, V. S. LeBleu, E. A. Mittendorf, J. Weitz, N. Rahbari, C. Reissfelder, C. Pilarsky, M. F. Fraga, D. Piwnica-Worms and R. Kalluri, *Nature*, 2015, **523**, 177–182.
27 J. Inal, *Br. J. Haematol.*, 2020, **190**, e218–e220.
28 S. Cheng, Y. Li, H. Yan, Y. Wen, X. Zhou, L. Friedman and Y. Zeng, *Lab Chip*, 2021, **21**, 3219–3243.
29 K. S. Yang, H. Im, S. Hong, I. Pergolini, A. F. Del Castillo, R. Wang, S. Clardy, C. H. Huang, C. Pille, S. Ferrone, R. Yang, C. M. Castro, H. Lee, C. F. Del Castillo and R. Weissleder, *Sci. Transl. Med.*, 2017, **9**, eaal3226.
30 K. Liang, F. Liu, J. Fan, D. Sun, C. Liu, C. J. Lyon, D. W. Bernard, Y. Li, K. Yokoi, M. H. Katz, E. J. Koay, Z. Zhao and Y. Hu, *Nat. Biomed. Eng.*, 2017, **1**, 0021.
31 C. Z. J. Lim, Y. Zhang, Y. Chen, H. Zhao, M. C. Stephenson, N. R. Y. Ho, Y. Chen, J. Chung, A. Reilhac, T. P. Loh, C. L. H. Chen and H. Shao, *Nat. Commun.*, 2019, **10**, 1144.
32 M. Guo, J. Wang, Y. Zhao, Y. Feng, S. Han, Q. Dong, M. Cui and K. Tieu, *Brain*, 2020, **143**, 1476–1497.
33 Y. Kwon and J. Park, *Micro Nano Syst. Lett.*, 2022, **10**, 14.
34 J. Lee, O. Sul and S. B. Lee, *Micromachines*, 2020, **11**, 481.
35 Y. Song, T. Tian, Y. Shi, W. Liu, Y. Zou, T. Khajvand, S. Wang, Z. Zhu and C. Yang, *Chem. Sci.*, 2017, **8**, 1736–1751.
36 P. Bankó, S. Y. Lee, V. Nagygyörgy, M. Zrínyi, C. H. Chae, D. H. Cho and A. Telekes, *J. Hematol. Oncol.*, 2019, **12**, 48.
37 A. C. Söderström, M. Nybo, C. Nielsen and P. J. Vinholt, *Clin. Chem. Lab. Med.*, 2016, **54**, 1913–1920.
38 C.-y. Chiang and C. Chen, *J. Biomed. Sci.*, 2019, **26**, 9.
39 I. V. Pivkin, Z. Peng, G. E. Karniadakis, P. A. Buffet, M. Dao and S. Suresh, *Proc. Natl. Acad. Sci. U. S. A.*, 2016, **113**, 7804–7809.
40 D. Di Carlo, *J. Lab. Autom.*, 2012, **17**, 32–42.
41 N. Kang, Q. Guo, E. Islamzada, H. Ma and M. D. Scott, *Integr. Biol.*, 2018, **10**, 207–217.

42 K. Crawford, A. DeWitt, S. Brierre, T. Caffery, T. Jagneaux, C. Thomas, M. Macdonald, H. Tse, A. Shah, D. Di Carlo and H. R. O'Neal, *Am. J. Respir. Crit. Care Med.*, 2018, **198**, 280–282.
43 C. Petchakup, H. Yang, L. Gong, L. He, H. M. Tay, R. Dalan, A. J. Chung, K. H. H. Li and H. W. Hou, *Small*, 2022, **18**, e2104822.
44 V. Faustino, R. O. Rodrigues, D. Pinho, E. Costa, A. Santos-Silva, V. Miranda, J. S. Amaral and R. Lima, *Micromachines*, 2019, **10**, 645.
45 S. Zhu, F. Jiang, Y. Han, N. Xiang and Z. Ni, *Analyst*, 2020, **145**, 7103–7124.
46 Y. Shen, Y. Yalikun and Y. Tanaka, *Sens. Actuators, B*, 2019, **282**, 268–281.
47 T. W. Murphy, Q. Zhang, L. B. Naler, S. Ma and C. Lu, *Analyst*, 2017, **143**, 60–80.
48 T. R. Carey, K. L. Cotner, B. Li and L. L. Sohn, *Wiley Interdiscip. Rev.: Nanomed. Nanobiotechnol.*, 2019, **11**, e1529.
49 T. Luo, L. Fan, R. Zhu and D. Sun, *Micromachines*, 2019, **10**, 104.
50 X. Lu, M. Tayebi and Y. Ai, *Electrophoresis*, 2021, **42**, 2281–2292.
51 N. Liu, C. Petchakup, H. M. Tay, K. H. H. Li and H. W. Hou, in *Applications of Microfluidic Systems in Biology and Medicine*, ed. M. Tokeshi, Springer Singapore, Singapore, 2019, pp. 99–150, DOI: **10.1007/978-981-13-6229-3_5**.
52 Y. Sun and P. Sethu, *Biomed. Microdevices*, 2018, **20**, 77.
53 S. Pandey, N. Mehendale and D. Paul, in *Handbook of Single-Cell Technologies*, ed. T. S. Santra and F.-G. Tseng, Springer Singapore, Singapore, 2022, pp. 207–234, DOI: **10.1007/978-981-10-8953-4_6**.
54 B. A. Sutermaster and E. M. Darling, *Sci. Rep.*, 2019, **9**, 227.
55 C. W. T. Shields, C. D. Reyes and G. P. Lopez, *Lab Chip*, 2015, **15**, 1230–1249.
56 S. A. Faraghat, K. F. Hoettges, M. K. Steinbach, D. R. van der Veen, W. J. Brackenbury, E. A. Henslee, F. H. Labeed and M. P. Hughes, *Proc. Natl. Acad. Sci. U. S. A.*, 2017, **114**, 4591–4596.
57 J. Stam, S. Bartel, R. Bischoff and J. C. Wolters, *J. Chromatogr., B*, 2021, **1169**, 122604.
58 M. Li, A. J. Rai, G. J. DeCastro, E. Zeringer, T. Barta, S. Magdaleno, R. Setterquist and A. V. Vlassov, *Methods*, 2015, **87**, 26–30.
59 B. J. Tauro, D. W. Greening, R. A. Mathias, H. Ji, S. Mathivanan, A. M. Scott and R. J. Simpson, *Methods*, 2012, **56**, 293–304.
60 T. Soares Martins, J. Catita, I. Martins Rosa, A. B. da Cruz E Silva Odete and A. G. Henriques, *PLoS One*, 2018, **13**, e0198820.
61 L. S. Gaspar, M. M. Santana, C. Henriques, M. M. Pinto, T. M. Ribeiro-Rodrigues, H. Girão, R. J. Nobre and L. Pereira de Almeida, *Mol. Ther.–Methods Clin. Dev.*, 2020, **18**, 723–737.
62 K. Sidhom, P. O. Obi and A. Saleem, *Int. J. Mol. Sci.*, 2020, **21**, 6466.
63 X. Fan, C. Jia, J. Yang, G. Li, H. Mao, Q. Jin and J. Zhao, *Biosens. Bioelectron.*, 2015, **71**, 380–386.
64 Y. T. Kang, I. Doh, J. Byun, H. J. Chang and Y. H. Cho, *Theranostics*, 2017, **7**, 3179–3191.
65 A. F. Sarioglu, N. Aceto, N. Kojic, M. C. Donaldson, M. Zeinali, B. Hamza, A. Engstrom, H. Zhu, T. K. Sundaresan, D. T. Miyamoto, X. Luo, A. Bardia, B. S. Wittner, S. Ramaswamy, T. Shioda, D. T. Ting, S. L. Stott, R. Kapur, S. Maheswaran, D. A. Haber and M. Toner, *Nat. Methods*, 2015, **12**, 685–691.
66 N. Mehendale, O. Sharma, S. Pandey and D. Paul, *Biomed. Microdevices*, 2018, **20**, 75.
67 A. Dalili, E. Samiei and M. Hoorfar, *Analyst*, 2018, **144**, 87–113.
68 W. Su, H. Li, W. Chen and J. Qin, *TrAC, Trends Anal. Chem.*, 2019, **118**, 686–698.
69 S. W. Lee, K. A. Hyun, S. I. Kim, J. Y. Kang and H. I. Jung, *J. Chromatogr. A*, 2015, **1377**, 100–105.
70 R. Ozawa, H. Iwadate, H. Toyoda, M. Yamada and M. Seki, *Lab Chip*, 2019, **19**, 1828–1837.
71 H. Xia, B. C. Strachan, S. C. Gifford and S. S. Shevkoplyas, *Sci. Rep.*, 2016, **6**, 35943.
72 C. B. Raub, C. Lee and E. Kartalov, *Sens. Actuators, B*, 2015, **210**, 120–123.
73 M. Dehghani, K. Lucas, J. Flax, J. McGrath and T. Gaborski, *Adv. Mater. Technol.*, 2019, **4**, 1900539.
74 V. Riazanski, G. Mauleon, K. Lucas, S. Walker, A. M. Zimnicka, J. L. McGrath and D. J. Nelson, *Commun. Biol.*, 2022, **5**, 13.
75 Z. Han, C. Peng, J. Yi, D. Zhang, X. Xiang, X. Peng, B. Su, B. Liu, Y. Shen and L. Qiao, *Sens. Actuators, B*, 2021, **333**, 129563.
76 A. Hochstetter, R. Vernekar, R. H. Austin, H. Becker, J. P. Beech, D. A. Fedosov, G. Gompper, S. C. Kim, J. T. Smith, G. Stolovitzky, J. O. Tegenfeldt, B. H. Wunsch, K. K. Zeming, T. Kruger and D. W. Inglis, *ACS Nano*, 2020, **14**, 10784–10795.
77 J. T. Smith, B. H. Wunsch, N. Dogra, M. E. Ahsen, K. Lee, K. K. Yadav, R. Weil, M. A. Pereira, J. V. Patel, E. A. Duch, J. M. Papalia, M. F. Lofaro, M. Gupta, A. K. Tewari, C. Cordon-Cardo, G. Stolovitzky and S. M. Gifford, *Lab Chip*, 2018, **18**, 3913–3925.
78 K. K. Zeming, T. Salafi, C. H. Chen and Y. Zhang, *Sci. Rep.*, 2016, **6**, 22934.
79 S. H. Au, J. Edd, A. E. Stoddard, K. H. K. Wong, F. Fachin, S. Maheswaran, D. A. Haber, S. L. Stott, R. Kapur and M. Toner, *Sci. Rep.*, 2017, **7**, 2433.
80 H. Okano, T. Konishi, T. Suzuki, T. Suzuki, S. Ariyasu, S. Aoki, R. Abe and M. Hayase, *Biomed. Microdevices*, 2015, **17**, 9964.
81 T. Jing, Z. Lai, L. Wu, J. Han, C. T. Lim and C. H. Chen, *Anal. Chem.*, 2016, **88**, 11750–11757.
82 N. Tottori and T. Nisisako, *Anal. Chem.*, 2019, **91**, 3093–3100.
83 K. K. Zeming, R. Vernekar, M. T. Chua, K. Y. Quek, G. Sutton, T. Kruger, W. S. Kuan and J. Han, *Small*, 2021, **17**, e2006123.
84 E. Pariset, C. Parent, Y. Fouillet, B. Francois, N. Verplanck, F. Revol-Cavalier, A. Thuaire and V. Agache, *Sci. Rep.*, 2018, **8**, 17762.

85 L. R. Huang, E. C. Cox, R. H. Austin and J. C. Sturm, *Science*, 2004, **304**, 987–990.
86 T. S. H. Tran, B. D. Ho, J. P. Beech and J. O. Tegenfeldt, *Lab Chip*, 2017, **17**, 3592–3600.
87 D. Huang, J. Man, D. Jiang, J. Zhao and N. Xiang, *Electrophoresis*, 2020, **41**, 2166–2187.
88 Y. Gou, Y. Jia, P. Wang and C. Sun, *Sensors*, 2018, **18**, 1762.
89 J. Zhang, S. Yan, D. Yuan, G. Alici, N. T. Nguyen, M. Ebrahimi Warkiani and W. Li, *Lab Chip*, 2016, **16**, 10–34.
90 A. S. Rzhevskiy, S. Razavi Bazaz, L. Ding, A. Kapitannikova, N. Sayyadi, D. Campbell, B. Walsh, D. Gillatt, M. Ebrahimi Warkiani and A. V. Zvyagin, *Cancers*, 2020, **12**, 81.
91 A. Rahi, M. Kazemi, E. Pishbin, S. Karimi and H. Nazarian, *Analyst*, 2021, **146**, 7230–7239.
92 J. M. Martel and M. Toner, *Annu. Rev. Biomed. Eng.*, 2014, **16**, 371–396.
93 A. Abdulla, T. Zhang, K. Z. Ahmad, S. Li, J. Lou and X. Ding, *Anal. Chem.*, 2020, **92**, 16170–16179.
94 J. Zhou, A. Kulasinghe, A. Bogseth, K. O'Byrne, C. Punyadeera and I. Papautsky, *Microsyst. Nanoeng.*, 2019, **5**, 8.
95 S. Zhu, D. Wu, Y. Han, C. Wang, N. Xiang and Z. Ni, *Lab Chip*, 2020, **20**, 244–252.
96 H. M. Tay, S. Kharel, R. Dalan, Z. J. Chen, K. K. Tan, B. O. Boehm, S. C. J. Loo and H. W. Hou, *NPG Asia Mater.*, 2017, **9**, e434.
97 H. M. Tay, S. Y. Leong, X. Xu, F. Kong, M. Upadya, R. Dalan, C. Y. Tay, M. Dao, S. Suresh and H. W. Hou, *Lab Chip*, 2021, **21**, 2511–2523.
98 B. Kim, S. S. Lee, T. H. Yoo and J. M. Kim, *Electrophoresis*, 2021, **42**, 2238–2245.
99 C. Liu, J. Guo, F. Tian, N. Yang, F. Yan, Y. Ding, J. Wei, G. Hu, G. Nie and J. Sun, *ACS Nano*, 2017, **11**, 6968–6976.
100 J. Nam, J. Yoon, H. Jee, W. S. Jang and C. S. Lim, *Adv. Mater. Technol.*, 2020, **5**, 2000612.
101 I. Bilican, *J. Chromatogr. A*, 2021, **1652**, 462366.
102 M. A. Faridi, H. Ramachandraiah, I. Banerjee, S. Ardabili, S. Zelenin and A. Russom, *J. Nanobiotechnol.*, 2017, **15**, 3.
103 D. Yuan, S. Yadav, H. T. Ta, H. Fallahi, H. An, N. Kashaninejad, C. H. Ooi, N.-T. Nguyen and J. Zhang, *Electrophoresis*, 2021, **42**, 2230–2237.
104 T. Kumar, H. Ramachandraiah, S. N. Iyengar, I. Banerjee, G. Mårtensson and A. Russom, *Sci. Rep.*, 2021, **11**, 8467.
105 J. Zhou and I. Papautsky, *Microsyst. Nanoeng.*, 2020, **6**, 113.
106 M. Wu, A. Ozcelik, J. Rufo, Z. Wang, R. Fang and T. Jun Huang, *Microsyst. Nanoeng.*, 2019, **5**, 1–18.
107 J. Rufo, F. Cai, J. Friend, M. Wiklund and T. J. Huang, *Nat. Rev. Dis. Primers*, 2022, **2**, 1–21.
108 Y. Zhou, Z. Ma and Y. Ai, *RSC Adv.*, 2019, **9**, 31186–31195.
109 K. Wang, W. Zhou, Z. Lin, F. Cai, F. Li, J. Wu, L. Meng, L. Niu and H. Zheng, *Sens. Actuators, B*, 2018, **258**, 1174–1183.
110 M. Antfolk, C. Magnusson, P. Augustsson, H. Lilja and T. Laurell, *Anal. Chem.*, 2015, **87**, 9322–9328.
111 C. Magnusson, P. Augustsson, A. Lenshof, Y. Ceder, T. Laurell and H. Lilja, *Anal. Chem.*, 2017, **89**, 11954–11961.
112 K. Cushing, E. Undvall, Y. Ceder, H. Lilja and T. Laurell, *Anal. Chim. Acta*, 2018, **1000**, 256–264.
113 Y. Gu, C. Chen, Z. Wang, P. H. Huang, H. Fu, L. Wang, M. Wu, Y. Chen, T. Gao, J. Gong, J. Kwun, G. M. Arepally and T. J. Huang, *Lab Chip*, 2019, **19**, 394–402.
114 C. Richard, A. Fakhfouri, M. Colditz, F. Striggow, R. Kronstein-Wiedemann, T. Tonn, M. Medina-Sánchez, O. G. Schmidt, T. Gemming and A. Winkler, *Lab Chip*, 2019, **19**, 4043–4051.
115 P. Ohlsson, K. Petersson, P. Augustsson and T. Laurell, *Sci. Rep.*, 2018, **9**, 9156.
116 C. Devendran, K. Choi, J. Han, Y. Ai, A. Neild and D. J. Collins, *Lab Chip*, 2020, **20**, 2674–2688.
117 M. Wu, Y. Ouyang, Z. Wang, R. Zhang, P. H. Huang, C. Chen, H. Li, P. Li, D. Quinn, M. Dao, S. Suresh, Y. Sadovsky and T. J. Huang, *Proc. Natl. Acad. Sci. U. S. A.*, 2017, **114**, 10584–10589.
118 L. Velmanickam, V. Jayasooriya, M. S. Vemuri, U. R. Tida and D. Nawarathna, *Electrophoresis*, 2022, **43**, 212–231.
119 B. Sarno, D. Heineck, M. J. Heller and S. D. Ibsen, *Electrophoresis*, 2021, **42**, 539–564.
120 G. I. Russo, N. Musso, A. Romano, G. Caruso, S. Petralia, L. Lanzanò, G. Broggi and M. Camarda, *Cancers*, 2021, **14**, 198.
121 P. Balasubramanian, R. J. Kinders, S. Kummar, V. Gupta, D. Hasegawa, A. Menachery, S. M. Lawrence, L. Wang, K. Ferry-Galow and D. Davis, *PLoS One*, 2017, **12**, e0175414.
122 A. Alazzam, B. Mathew and F. Alhammadi, *J. Sep. Sci.*, 2017, **40**, 1193–1200.
123 M. Dudaie, N. Nissim, I. Barnea, T. Gerling, C. Duschl, M. Kirschbaum and N. T. Shaked, *J. Biophotonics*, 2020, **13**, e202000151.
124 J. L. Prieto, H.-W. Su, H. W. Hou, M. P. Vera, B. D. Levy, R. M. Baron, J. Han and J. Voldman, *Lab Chip*, 2016, **16**, 4333–4340.
125 L. D'Amico, N. Ajami, J. Adachi, P. Gascoyne and J. Petrosino, *Lab Chip*, 2017, **17**, 1340–1348.
126 E. Bisceglia, M. Cubizolles, C. I. Trainito, J. Berthier, C. Pudda, O. Français, F. Mallard and B. Le Pioufle, *Sens. Actuators, B*, 2015, **212**, 335–343.
127 K.-H. Chen, S.-H. Lee, L.-C. Kok, T.-O. Ishdorj, H.-Y. Chang and F.-G. Tseng, *Biosens. Bioelectron.*, 2022, **197**, 113740.
128 S. D. Ibsen, J. Wright, J. M. Lewis, S. Kim, S.-Y. Ko, J. Ong, S. Manouchehri, A. Vyas, J. Akers and C. C. Chen, *ACS Nano*, 2017, **11**, 6641–6651.
129 J. M. Lewis, A. D. Vyas, Y. Qiu, K. S. Messer, R. White and M. J. Heller, *ACS Nano*, 2018, **12**, 3311–3320.
130 M. Tayebi, D. Yang, D. J. Collins and Y. Ai, *Nano Lett.*, 2021, **21**, 6835–6842.
131 F. Yang, Y. Zhang, X. Cui, Y. Fan, Y. Xue, H. Miao and G. Li, *Biotechnol. J.*, 2019, **14**, 1800181.
132 Y. Li, Y. Wang, K. Wan, M. Wu, L. Guo, X. Liu and G. Wei, *Nanoscale*, 2021, **13**, 4330–4358.
133 B. R. Mutlu, K. C. Smith, J. F. Edd, P. Nadar, M. Dlamini, R. Kapur and M. Toner, *Sci. Rep.*, 2017, **7**, 9915.
134 J. Zhou, C. Tu, Y. Liang, B. Huang, Y. Fang, X. Liang, I. Papautsky and X. Ye, *Sci. Rep.*, 2018, **8**, 9411.

135 J. Zhou and I. Papautsky, *Lab Chip*, 2019, **19**, 3416–3426.
136 M. Li, C. Ge, Y. Yang, M. Gan, Y. Xu, L. Chen and S. Li, *Anal. Bioanal. Chem.*, 2022, **414**, 7683–7694.
137 J. Che, V. Yu, M. Dhar, C. Renier, M. Matsumoto, K. Heirich, E. B. Garon, J. Goldman, J. Rao, G. W. Sledge, M. D. Pegram, S. Sheth, S. S. Jeffrey, R. P. Kulkarni, E. Sollier and D. Di Carlo, *Oncotarget*, 2016, **7**, 12748–12760.
138 M. Dhar, J. N. Lam, T. Walser, S. M. Dubinett, M. B. Rettig and D. Di Carlo, *Proc. Natl. Acad. Sci. U. S. A.*, 2018, **115**, 9986–9991.
139 M. Dhar, J. Wong, A. Karimi, J. Che, C. Renier, M. Matsumoto, M. Triboulet, E. B. Garon, J. W. Goldman, M. B. Rettig, S. S. Jeffrey, R. P. Kulkarni, E. Sollier and D. Di Carlo, *Biomicrofluidics*, 2015, **9**, 064116.
140 E. Sollier, D. E. Go, J. Che, D. R. Gossett, S. O'Byrne, W. M. Weaver, N. Kummer, M. Rettig, J. Goldman, N. Nickols, S. McCloskey, R. P. Kulkarni and D. Di Carlo, *Lab Chip*, 2014, **14**, 63–77.
141 M. S. Bhamla, B. Benson, C. Chai, G. Katsikis, A. Johri and M. Prakash, *Nat. Biomed. Eng.*, 2017, **1**, 0009.
142 M. S. Maria, P. E. Rakesh, T. S. Chandra and A. K. Sen, *Sci. Rep.*, 2017, **7**, 43457.
143 A. Shamloo and M. Besanjideh, *IEEE Trans. Biomed. Eng.*, 2020, **67**, 372–378.
144 Y. Liu, W. Zhao, R. Cheng, B. N. Harris, J. R. Murrow, J. Hodgson, M. Egan, A. Bankey, P. G. Nikolinakos, T. Laver, K. Meichner and L. Mao, *Lab Chip*, 2021, **21**, 1706–1723.
145 W. Zhao, R. Cheng, S. H. Lim, J. R. Miller, W. Zhang, W. Tang, J. Xie and L. Mao, *Lab Chip*, 2017, **17**, 2243–2255.
146 W. Zhao, T. Zhu, R. Cheng, Y. Liu, J. He, H. Qiu, L. Wang, T. Nagy, T. D. Querec, E. R. Unger and L. Mao, *Adv. Funct. Mater.*, 2016, **26**, 3990–3998.
147 W. Zhao, R. Cheng, J. R. Miller and L. Mao, *Adv. Funct. Mater.*, 2016, **26**, 3916–3932.
148 M. Frenea-Robin and J. Marchalot, *Magnetochemistry*, 2022, **8**, 11.
149 J. Zeng, Y. Deng, P. Vedantam, T.-R. Tzeng and X. Xuan, *J. Magn. Magn. Mater.*, 2013, **346**, 118–123.
150 A. R. Kose, B. Fischer, L. Mao and H. Koser, *Proc. Natl. Acad. Sci. U. S. A.*, 2009, **106**, 21478–21483.
151 C.-D. Xue, J.-M. Zhao, Z.-P. Sun, J.-T. Na, Y.-J. Li and K.-R. Qin, *Microfluid. Nanofluid.*, 2021, **25**, 97.
152 T. H. Kim, M. Lim, J. Park, J. M. Oh, H. Kim, H. Jeong, S. J. Lee, H. C. Park, S. Jung, B. C. Kim, K. Lee, M. H. Kim, D. Y. Park, G. H. Kim and Y. K. Cho, *Anal. Chem.*, 2017, **89**, 1155–1162.
153 H. Pei, L. Li, Z. Han, Y. Wang and B. Tang, *Lab Chip*, 2020, **20**, 3854–3875.
154 L. Guillou, R. Sheybani, A. E. Jensen, D. Di Carlo, T. S. Caffery, C. B. Thomas, A. M. Shah, H. T. K. Tse and H. R. O'Neal, Jr., *PLoS One*, 2021, **16**, e0246980.
155 D. Rossi, D. Dannhauser, M. Telesco, P. A. Netti and F. Causa, *Lab Chip*, 2019, **19**, 3888–3898.
156 I. W. Schie, J. Ruger, A. S. Mondol, A. Ramoji, U. Neugebauer, C. Krafft and J. Popp, *Anal. Chem.*, 2018, **90**, 2023–2030.
157 A. A. Sina, R. Vaidyanathan, S. Dey, L. G. Carrascosa, M. J. Shiddiky and M. Trau, *Sci. Rep.*, 2016, **6**, 30460.
158 J. Su, *ACS Photonics*, 2015, **2**, 1241–1245.
159 M. Ugele, M. Weniger, M. Stanzel, M. Bassler, S. W. Krause, O. Friedrich, O. Hayden and L. Richter, *Adv. Sci.*, 2018, **5**, 1800761.
160 J. Yoon, Y. Jo, M. H. Kim, K. Kim, S. Lee, S. J. Kang and Y. Park, *Sci. Rep.*, 2017, **7**, 6654.
161 Y. Yang, G. Shen, H. Wang, H. Li, T. Zhang, N. Tao, X. Ding and H. Yu, *Proc. Natl. Acad. Sci. U. S. A.*, 2018, **115**, 10275–10280.
162 K. C. M. Lee, M. Wang, K. S. E. Cheah, G. C. F. Chan, H. K. H. So, K. K. Y. Wong and K. K. Tsia, *Cytometry*, 2019, **95**, 510–520.
163 D. H. Lee, X. Li, N. Ma, M. A. Digman and A. P. Lee, *Lab Chip*, 2018, **18**, 1349–1358.
164 J. Gala de Pablo, M. Lindley, K. Hiramatsu and K. Goda, *Acc. Chem. Res.*, 2021, **54**, 2132–2143.
165 H. W. Wang, N. Bao, T. L. Le, C. Lu and J. X. Cheng, *Opt. Express*, 2008, **16**, 5782–5789.
166 N. Nitta, T. Sugimura, A. Isozaki, H. Mikami, K. Hiraki, S. Sakuma, T. Iino, F. Arai, T. Endo, Y. Fujiwaki, H. Fukuzawa, M. Hase, T. Hayakawa, K. Hiramatsu, Y. Hoshino, M. Inaba, T. Ito, H. Karakawa, Y. Kasai, K. Koizumi, S. Lee, C. Lei, M. Li, T. Maeno, S. Matsusaka, D. Murakami, A. Nakagawa, Y. Oguchi, M. Oikawa, T. Ota, K. Shiba, H. Shintaku, Y. Shirasaki, K. Suga, Y. Suzuki, N. Suzuki, Y. Tanaka, H. Tezuka, C. Toyokawa, Y. Yalikun, M. Yamada, M. Yamagishi, T. Yamano, A. Yasumoto, Y. Yatomi, M. Yazawa, D. Di Carlo, Y. Hosokawa, S. Uemura, Y. Ozeki and K. Goda, *Cell*, 2018, **175**, 266–276, e213.
167 M. Lindley, J. Gala de Pablo, W. Peterson, A. Isozaki, K. Hiramatsu and K. Goda, *Adv. Mater. Technol.*, 2022, **7**, 2101567.
168 C. Zhang, K.-C. Huang, B. Rajwa, J. Li, S. Yang, H. Lin, C.-s. Liao, G. Eakins, S. Kuang, V. Patsekin, J. P. Robinson and J.-X. Cheng, *Optica*, 2017, **4**, 103–109.
169 Y. Suzuki, K. Kobayashi, Y. Wakisaka, D. Deng, S. Tanaka, C. J. Huang, C. Lei, C. W. Sun, H. Liu, Y. Fujiwaki, S. Lee, A. Isozaki, Y. Kasai, T. Hayakawa, S. Sakuma, F. Arai, K. Koizumi, H. Tezuka, M. Inaba, K. Hiraki, T. Ito, M. Hase, S. Matsusaka, K. Shiba, K. Suga, M. Nishikawa, M. Jona, Y. Yatomi, Y. Yalikun, Y. Tanaka, T. Sugimura, N. Nitta, K. Goda and Y. Ozeki, *Proc. Natl. Acad. Sci. U. S. A.*, 2019, **116**, 15842–15848.
170 C. Rianna and M. Radmacher, *AIP Conf. Proc.*, 2016, **1760**, 020057.
171 O. Otto, P. Rosendahl, A. Mietke, S. Golfier, C. Herold, D. Klaue, S. Girardo, S. A.-O. Pagliara, A. Ekpenyong, A. Jacobi, M. Wobus, N. Töpfner, U. F. Keyser, J. Mansfeld, E. Fischer-Friedrich and J. Guck, *Nat. Methods*, 2015, **12**, 199–202.
172 Y. Deng, S. P. Davis, F. Yang, K. S. Paulsen, M. Kumar, R. Sinnott DeVaux, X. Wang, D. S. Conklin, A. Oberai, J. I. Herschkowitz and A. J. Chung, *Small*, 2017, **13**, 1700705.
173 A. Menachery, J. Sapudom, A. Vembadi, A. Alatoom, J. Teo and M. A. Qasaimeh, *BioTechniques*, 2020, **70**, 29–36.

174 J. Che, V. Yu, E. B. Garon, J. W. Goldman and D. Di Carlo, *Lab Chip*, 2017, **17**, 1452–1461.
175 M. Urbanska, H. E. Muñoz, J. Shaw Bagnall, O. Otto, S. R. Manalis, D. Di Carlo and J. Guck, *Nat. Methods*, 2020, **17**, 587–593.
176 M. Kubánková, B. Hohberger, J. Hoffmanns, J. Fürst, M. Herrmann, J. Guck and M. Kräter, *Biophys. J.*, 2021, **120**, 2838–2847.
177 K. D. Nyberg, K. H. Hu, S. H. Kleinman, D. B. Khismatullin, M. J. Butte and A. C. Rowat, *Biophys. J.*, 2017, **113**, 1574–1584.
178 C. Petchakup, H. Yang, L. Gong, L. He, H. M. Tay, R. Dalan, A. J. Chung, K. H. H. Li and H. W. Hou, *Small*, 2022, **18**, 2104822.
179 Y. Feng, H. Chai, W. He, F. Liang, Z. Cheng and W. Wang, *Small Methods*, 2022, 2200325.
180 A. A.-O. Ekpenyong, N. Toepfner, C. Fiddler, M. Herbig, W. Li, G. Cojoc, C. Summers, J. Guck and E. A.-O. Chilvers, *Sci. Adv.*, 2017, **3**, 2375–2548.
181 J. Shaw Bagnall, S. Byun, S. Begum, D. T. Miyamoto, V. C. Hecht, S. Maheswaran, S. L. Stott, M. Toner, R. O. Hynes and S. R. Manalis, *Sci. Rep.*, 2015, **5**, 18542.
182 Y. Zhou, D. Yang, Y. Zhou, B. L. Khoo, J. Han and Y. Ai, *Anal. Chem.*, 2018, **90**, 912–919.
183 M.-E. Myrand-Lapierre, X. Deng, R. R. Ang, K. Matthews, A. T. Santoso and H. Ma, *Lab Chip*, 2015, **15**, 159–167.
184 Q. Guo, S. P. Duffy, K. Matthews, E. Islamzada and H. Ma, *Sci. Rep.*, 2017, **7**, 6627.
185 Y. Man, D. Maji, R. An, S. P. Ahuja, J. A. Little, M. A. Suster, P. Mohseni and U. A. Gurkan, *Lab Chip*, 2021, **21**, 1036–1048.
186 D. Holmes, D. Pettigrew, C. H. Reccius, J. D. Gwyer, C. van Berkel, J. Holloway, D. E. Davies and H. Morgan, *Lab Chip*, 2009, **9**, 2881–2889.
187 A. De Ninno, R. Reale, A. Giovinazzo, F. R. Bertani, L. Businaro, P. Bisegna, C. Matteucci and F. Caselli, *Biosens. Bioelectron.*, 2020, **150**, 111887.
188 C. Petchakup, H. M. Tay, W. H. Yeap, R. Dalan, S. C. Wong, K. H. H. Li and H. W. Hou, *Biosens. Bioelectron.*, 2018, **118**, 195–203.
189 C. Petchakup, H. M. Tay, K. H. H. Li and H. W. Hou, *Lab Chip*, 2019, **19**, 1736–1746.
190 J. Zhong, Q. Tang, M. Liang and Y. Ai, *Sens. Actuators, B*, 2022, **367**, 132068.
191 J. Zhong, M. Liang and Y. Ai, *Lab Chip*, 2021, **21**, 2869–2880.
192 S. Subramaniam, U. Ahmed, S. Benerjee, P. Jain and P. Chowdhury, *2019 11th International Conference on Communication Systems & Networks (COMSNETS)*, Bengaluru, India, 2019, pp. 829–832.
193 P. Simon, M. Frankowski, N. Bock and J. Neukammer, *Lab Chip*, 2016, **16**, 2326–2338.
194 K. Mahesh, M. Varma and P. Sen, *Lab Chip*, 2020, **20**, 4296–4309.
195 C. Honrado, L. Ciuffreda, D. Spencer, L. Ranford-Cartwright and H. Morgan, *J. R. Soc., Interface*, 2018, **15**, 20180416.
196 S.-I. Han and K.-H. Han, *Anal. Chem.*, 2015, **87**, 10585–10592.
197 S. A. Hosseini, M. Abdolahad, S. Zanganeh, M. Dahmardeh, M. Gharooni, H. Abiri, A. Alikhani, S. Mohajerzadeh and O. Mashinchian, *Small*, 2016, **12**, 883–891.
198 C. Raillon, J. Che, S. Thill, M. Duchamp, B. X. E. Desbiolles, A. Millet, E. Sollier and P. Renaud, *Cytometry, Part A*, 2019, **95**, 1085–1095.
199 J. Liu, Y. Qiang, O. Alvarez and E. Du, *Sens. Actuators, B*, 2018, **255**, 2392–2398.
200 M. Leclercq, B. Vittrant, M. L. Martin-Magniette, M. P. Scott Boyer, O. Perin, A. Bergeron, Y. Fradet and A. Droit, *Front. Genet.*, 2019, **10**, 452.
201 P. Rajpurkar, E. Chen, O. Banerjee and E. J. Topol, *Nat. Med.*, 2022, **28**, 31–38.
202 D. McIntyre, A. Lashkaripour, P. Fordyce and D. Densmore, *Lab Chip*, 2022, **22**, 2925–2937.
203 J. Zheng, T. Cole, Y. Zhang, J. Kim and S.-Y. Tang, *Biosens. Bioelectron.*, 2021, **194**, 113666.
204 A. Isozaki, J. Harmon, Y. Zhou, S. Li, Y. Nakagawa, M. Hayashi, H. Mikami, C. Lei and K. Goda, *Lab Chip*, 2020, **20**, 3074–3090.
205 K. C. M. Lee, J. Guck, K. Goda and K. K. Tsia, *Trends Biotechnol.*, 2021, **39**, 1249–1262.
206 L. Alzubaidi, J. Zhang, A. J. Humaidi, A. Al-Dujaili, Y. Duan, O. Al-Shamma, J. Santamaría, M. A. Fadhel, M. Al-Amidie and L. Farhan, *J. Big Data*, 2021, **8**, 53.
207 Y. LeCun, Y. Bengio and G. Hinton, *Nature*, 2015, **521**, 436–444.
208 J. J. Bird, J. Kobylarz, D. R. Faria, A. Ekárt and E. P. Ribeiro, *IEEE Access*, 2020, **8**, 54789–54801.
209 M. Kräter, S. Abuhattum, D. Soteriou, A. Jacobi, T. Krüger, J. Guck and M. Herbig, *Adv. Sci.*, 2021, **8**, 2003743.
210 H. Kobayashi, C. Lei, Y. Wu, C.-J. Huang, A. Yasumoto, M. Jona, W. Li, Y. Wu, Y. Yalikun, Y. Jiang, B. Guo, C.-W. Sun, Y. Tanaka, M. Yamada, Y. Yatomi and K. Goda, *Lab Chip*, 2019, **19**, 2688–2698.
211 C. Combs, D. D. Seith, M. J. Bovyn, S. P. Gross, X. Xie and Z. S. Siwy, *Biomicrofluidics*, 2022, **16**, 014104.
212 F. Caselli, R. Reale, A. De Ninno, D. Spencer, H. Morgan and P. Bisegna, *Lab Chip*, 2022, **22**, 1714–1722.
213 C. Honrado, J. S. McGrath, R. Reale, P. Bisegna, N. S. Swami and F. Caselli, *Anal. Bioanal. Chem.*, 2020, **412**, 3835–3845.
214 N. Wang, R. Liu, N. Asmare, C.-H. Chu and A. F. Sarioglu, *Lab Chip*, 2019, **19**, 3292–3304.
215 M. Wang, J. Zhang, H. Tan, D. Chen, Y. Lei, Y. Li, J. Wang and J. Chen, *Cytometry*, 2022, **101**, 639–647.
216 H. Tan, M. Wang, Y. Zhang, X. Huang, D. Chen, Y. Li, M.-H. Wu, K. Wang, J. Wang and J. Chen, *Cytometry*, 2022, **101**, 630–638.
217 D. K. Singh, C. C. Ahrens, W. Li and S. A. Vanapalli, *Lab Chip*, 2017, **17**, 2920–2932.
218 K. K. Zeming, R. Vernekar, M. T. Chua, K. Y. Quek, G. Sutton, T. Krüger, W. S. Kuan and J. Han, *Small*, 2021, **17**, 2006123.
219 D. M. D. Siu, K. C. M. Lee, M. C. K. Lo, S. V. Stassen, M. Wang, I. Z. Q. Zhang, H. K. H. So, G. C. F. Chan, K. S. E.

Cheah, K. K. Y. Wong, M. K. Y. Hsin, J. C. M. Ho and K. K. Tsia, *Lab Chip*, 2020, **20**, 3696–3708.
220 J. Amann, A. Blasimme, E. Vayena, D. Frey, V. I. Madai and Q. c. the Precise, *BMC Med. Inf. Decis. Making*, 2020, **20**, 310.
221 B. Rozemberczki, L. Watson, P. Bayer, H.-T. Yang, O. Kiss, S. Nilsson and R. Sarkar, *arXiv*, 2022, preprint, arXiv:2202.05594.
222 A. Altmann, L. Toloși, O. Sander and T. Lengauer, *Bioinformatics*, 2010, **26**, 1340–1347.
223 R. R. Selvaraju, M. Cogswell, A. Das, R. Vedantam, D. Parikh and D. Batra, *Proceedings of the IEEE International Conference on Computer Vision (ICCV)*, 2017, pp. 618–626.
224 M. Herbig, A. Mietke, P. Müller and O. Otto, *Biomicrofluidics*, 2018, **12**, 042214.
225 D. Kobak and P. Berens, *Nat. Commun.*, 2019, **10**, 5416.
226 M. W. Dorrity, L. M. Saunders, C. Queitsch, S. Fields and C. Trapnell, *Nat. Commun.*, 2020, **11**, 1537.
227 V. Rizzuto, A. Mencattini, B. Álvarez-González, D. Di Giuseppe, E. Martinelli, D. Beneitez-Pastor, M. D. M. Mañú-Pereira, M. J. Lopez-Martinez and J. Samitier, *Sci. Rep.*, 2021, **11**, 13553.
228 Y. Rivenson, H. Wang, Z. Wei, K. de Haan, Y. Zhang, Y. Wu, H. Günaydın, J. E. Zuckerman, T. Chong, A. E. Sisk, L. M. Westbrook, W. D. Wallace and A. Ozcan, *Nat. Biomed. Eng.*, 2019, **3**, 466–477.
229 X. Yi, E. Walia and P. Babyn, *Med. Image Anal.*, 2019, **58**, 101552.
230 P. F. Virgo and G. J. Gibbs, *Ann. Clin. Biochem.*, 2012, **49**, 17–28.
231 C. Petchakup, P. E. Hutchinson, H. M. Tay, S. Y. Leong, K. H. H. Li and H. W. Hou, *Sens. Actuators, B*, 2021, **339**, 129864.
232 C. Raillon, J. Che, S. Thill, M. Duchamp, B. X. E. Desbiolles, A. Millet, E. Sollier and P. Renaud, *Cytometry, Part A*, 2019, **95**, 1085–1095.
233 P. Han, S. Yosinski, Z. A. Kobos, R. Chaudhury, J. S. Lee, T. M. Fahmy and M. A. Reed, *ACS Nano*, 2020, **14**, 8646–8657.
234 U. Hassan, N. N. Watkins, B. Reddy, G. Damhorst and R. Bashir, *Nat. Protoc.*, 2016, **11**, 714–726.
235 J. Zhong, P. Li, M. Liang and Y. Ai, *Adv. Mater. Technol.*, 2022, **7**, 2100906.
236 Y. Cheng, X. Ye, Z. Ma, S. Xie and W. Wang, *Biomicrofluidics*, 2016, **10**, 014118.
237 M. Yamada, W. Seko, T. Yanai, K. Ninomiya and M. Seki, *Lab Chip*, 2017, **17**, 304–314.
238 H. Chen, *Sci. Rep.*, 2018, **8**, 4042.
239 M. Wu, P. H. Huang, R. Zhang, Z. Mao, C. Chen, G. Kemeny, P. Li, A. V. Lee, R. Gyanchandani and A. J. Armstrong, *Small*, 2018, **14**, 1801131.
240 Y. Gu, C. Chen, Z. Wang, P.-H. Huang, H. Fu, L. Wang, M. Wu, Y. Chen, T. Gao and J. Gong, *Lab Chip*, 2019, **19**, 394–402.
241 Y. Chen, M. Wu, L. Ren, J. Liu, P. H. Whitley, L. Wang and T. J. Huang, *Lab Chip*, 2016, **16**, 3466–3472.
242 P. Ohlsson, K. Petersson, P. Augustsson and T. Laurell, *Sci. Rep.*, 2018, **8**, 1–11.
243 M. Wu, C. Chen, Z. Wang, H. Bachman, Y. Ouyang, P.-H. Huang, Y. Sadovsky and T. J. Huang, *Lab Chip*, 2019, **19**, 1174–1182.
244 M. Wu, Y. Ouyang, Z. Wang, R. Zhang, P.-H. Huang, C. Chen, H. Li, P. Li, D. Quinn and M. Dao, *Proc. Natl. Acad. Sci. U. S. A.*, 2017, **114**, 10584–10589.
245 S. M. Azarin, J. Yi, R. M. Gower, B. A. Aguado, M. E. Sullivan, A. G. Goodman, E. J. Jiang, S. S. Rao, Y. Ren, S. L. Tucker, V. Backman, J. S. Jeruss and L. D. Shea, *Nat. Commun.*, 2015, **6**, 8094.
246 M. Masaeli, D. Gupta, S. O'Byrne, H. T. K. Tse, D. R. Gossett, P. Tseng, A. S. Utada, H.-J. Jung, S. Young, A. T. Clark and D. Di Carlo, *Sci. Rep.*, 2016, **6**, 37863.
247 Y. Jiang, C. Lei, A. Yasumoto, H. Kobayashi, Y. Aisaka, T. Ito, B. Guo, N. Nitta, N. Kutsuna, Y. Ozeki, A. Nakagawa, Y. Yatomi and K. Goda, *Lab Chip*, 2017, **17**, 2426–2434.
248 T. Go, H. Byeon and S. J. Lee, *Biosens. Bioelectron.*, 2018, **103**, 12–18.
249 K. C. M. Lee, M. Wang, K. S. E. Cheah, G. C. F. Chan, H. K. H. So, K. K. Y. Wong and K. K. Tsia, *Cytometry, Part A*, 2019, **95**, 510–520.
250 A. A. Nawaz, M. Urbanska, M. Herbig, M. Nötzel, M. Kräter, P. Rosendahl, C. Herold, N. Toepfner, M. Kubánková, R. Goswami, S. Abuhattum, F. Reichel, P. Müller, A. Taubenberger, S. Girardo, A. Jacobi and J. Guck, *Nat. Methods*, 2020, **17**, 595–599.
251 M. Dudaie, N. Nissim, I. Barnea, T. Gerling, C. Duschl, M. Kirschbaum and N. T. Shaked, *J. Biophotonics*, 2020, **13**, e202000151.
252 D. Rossi, D. Dannhauser, M. Telesco, P. A. Netti and F. Causa, *Lab Chip*, 2019, **19**, 3888–3898.
253 A. A. Nawaz, M. Urbanska, M. Herbig, M. Nötzel, M. Kräter, P. Rosendahl, C. Herold, N. Toepfner, M. Kubánková, R. Goswami, S. Abuhattum, F. Reichel, P. Müller, A. Taubenberger, S. Girardo, A. Jacobi and J. Guck, *Nat. Methods*, 2020, **17**, 595–599.
254 N. Praljak, S. Iram, U. Goreke, G. Singh, A. Hill, U. A. Gurkan and M. Hinczewski, *PLoS Comput. Biol.*, 2021, **17**, e1008946.
255 E. S. Lamoureux, E. Islamzada, M. V. J. Wiens, K. Matthews, S. P. Duffy and H. Ma, *Lab Chip*, 2022, **22**, 26–39.
256 Y. Feng, Z. Cheng, H. Chai, W. He, L. Huang and W. Wang, *Lab Chip*, 2022, **22**, 240–249.
257 H. Jeon, M. Wei, X. Huang, J. Yao, W. Han, R. Wang, X. Xu, J. Chen, L. Sun and J. Han, *Anal. Chem.*, 2022, **94**, 6394–6402.